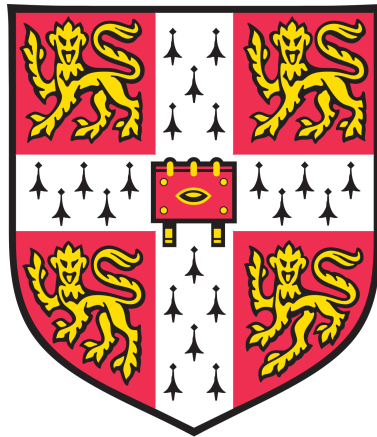


UNIVERSITY OF CAMBRIDGE
DEPARTMENT OF ENGINEERING

MASTERS PROJECT REPORT



Propulsion Systems for VTOL Electric Vehicles

Jordan Sandberg Eriksen

SUPERVISED BY: Dr Sam Grimshaw

Abstract

Abstract here..

Contents

1	Introduction	1
1.0.1	Figure of Merit	1
1.1	Literature Review	2
1.2	Research Questions	2
1.3	Approach	2
2	Flying Test Bed System Design	2
2.1	Flying Test Bed	2
2.1.1	Mechanical design	2
2.1.2	Customisation of <i>Pixhawk 4</i> flight hardware/software	4
2.1.3	Subsystem Functions	5
2.1.4	Subsystem Interaction	6
2.1.5	Telemetry	6
3	Ducted Fan Aerodynamic Design	7
3.1	Introduction	7
3.2	Mean-line Design	8
3.2.1	Non-dimensional Operating Point:	8
3.2.2	Fan Operating Speed:	8
3.2.3	Mean-line Location:	9
3.2.4	Overall Performance	9
3.2.5	Design Objectives and Constraints	9
3.2.6	ESDU 75026 Diffuser Data:	10
3.2.7	Mass Model	12
3.2.8	Design Selection	15
3.3	3D Blade Design	17
3.3.1	3-dimensional Flow Solutions to Radial Equilibrium:	17
3.3.2	3D Velocity Triangles:	20
3.3.3	Validation of Mean-line Location:	20
3.3.4	Blade Number and Span-wise Chord:	21
3.3.5	Deviation	24
3.3.6	Blade Lean	25
3.3.7	Noise	25
3.3.8	Blade Profiles	25
3.3.9	Design Selection	25

4 Electrical and Mechanical Design	26
4.1 Introduction	26
4.2 Electrical Design	26
4.2.1 Motor Requirements	26
4.2.2 Power Supply	26
4.2.3 Choice of Electric Motor	27
4.3 Mechanical Design	27
4.3.1 Propulsor Dimensions	27
4.3.2 Shrouded Rotor	28
4.3.3 Stator Block: Stator and Blade Duct Hub & Casing	30
4.3.4 Diffuser	30
4.3.5 Intake	31
4.3.6 3D Printing	31
5 Experimental Methods	33
5.1 Stationary Propulsor Test	33
5.1.1 Setup	34
5.1.2 Load-cell Calibration	35
5.2 Hover Test	35
5.2.1 Setup	36
5.2.2 Control	37
5.3 Measurement Techniques	37
5.3.1 Non-dimensional Quantities	37
5.3.2 Data Acquisition	38
5.3.3 Cage Design & Tether	38
6 Results	38
6.1 Stationary Propulsor Test	38
6.1.1 Comparison of Vortex Distributions	38
6.1.2 Version 1.0 EDF	38
6.1.3 Version 2.0 EDF	38
6.1.4 Version 3.0 EDF	38
6.1.5 Propeller	39
6.2 Hover Tests	39
6.2.1 Propeller Performance	39
6.2.2 Hover Test Limitations	39
7 Future Work	39
7.1 Propulsor Design	39
7.1.1 Stationary Propulsor Tests	39
7.1.2 Contra-rotating Ducted Fan	39
7.1.3 Computational Fluid Dynamics	39
7.2 Flying Test Bed Experiments	39

Nomenclature

e-VTOL	Test
FTB	Test
V_x	Axial flow velocity
Ω	
r_h	
r_c	
r_m	
U	
ϕ	Flow coefficient
ψ	Stage loading

Introduction

Intro and motivation

Consider Heilmeier when structuring this section.

- Integrate battery into casing, increase payload volume/utilise space

1.0.1 Figure of Merit

The effectiveness of a propulsor in hover can be measured by the figure of merit, M_F , defined as a non-dimensional thrust-to-power ratio

$$M_F = \frac{T}{P} \sqrt{\frac{T}{2\rho A_x}} \quad (1)$$

Where A_x , the blade passage axial flow area, can be related to the duct exit axial flow area, A_e , by the area ratio

$$\sigma = \frac{A_e}{A_x} \quad (2)$$

Considering the large control volume around the ducted fan in Fig. 1, the thrust generated by the fan can be determined from the steady flow momentum equation (SFME). Assuming zero inlet swirl and straight and parallel exit flow (zero exit swirl), the static pressure at the duct exit, p_e , is equal to atmospheric pressure, p_a . Continuity gives the relationship between duct exit velocity and area ratio

$$\dot{m} = \rho A_x V_x = \rho A_e V_e \quad \therefore \sigma = \frac{V_x}{V_e} \quad (3)$$

Therefore the SFME can be written in terms of the blade passage quantities (A_x and V_x) and the area ratio, σ

$$T = \dot{m}V_e \quad \therefore T = \frac{\rho A_x V_x^2}{\sigma} \quad (4)$$

Flow power is determined from the steady flow energy equation (SFEE)

$$P = \frac{1}{2}\dot{m}V_e^2 \quad \therefore P = \frac{\rho A_x V_x^3}{2\sigma^2} \quad (5)$$

Substituting Eqn. 4 and Eqn. 5 into Eqn. 1 gives a simplified expression for figure of merit of a ducted fan

$$M_F = \sqrt{2\sigma} \quad (6)$$

Therefore ducting the fan with an area ratio of $\sigma = 1$ gives a figure of merit of $M_F = \sqrt{2}$. Periera (2008)¹ shows the maximum figure of merit for a propeller to be 1. Provided the area ratio of the exit duct on a ducted fan remains $\sigma > 0.5$ the ducted fan figure of merit is greater. Therefore a small ducted fan is designed to determine whether the power required for static hover can be reduced compare to a propeller.

1.1 Literature Review

1.2 Research Questions

1.3 Approach

High level overview of what's been done and how the report is set out.

Flying Test Bed System Design

2.1 Flying Test Bed

A UROP was conducted in the summer preceding this project during which an axi-symmetric quadcopter flying test bed was designed and tested. The two challenges addressed were structural design of the chassis, and the customisation of flight control hardware and software. The UROP concluded with successful hover testing of the flying test bed. Off-the-shelf 10in. propellers were used in the test².

2.1.1 Mechanical design

The test bed was designed to be rapidly 3D printable, light weight – whilst maintaining structural integrity – and modular to allow various propulsors and instrumentation to be

¹REFERENCE PERIERA

²REFERENCE UROP REPORT

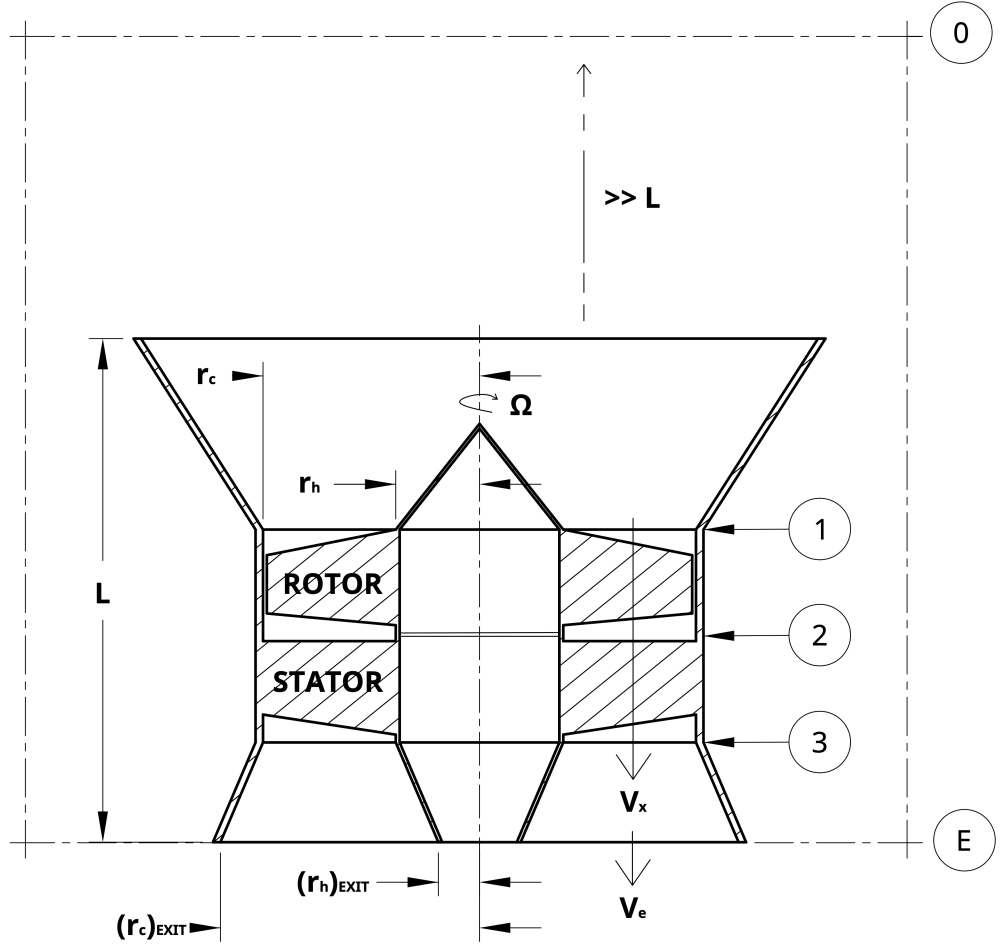


Figure 1: Ducted fan configuration and control volume. **0**: Control volume inlet plane; **1**: Rotor inlet plane; **2**: Inter-rotor-stator plane; **3**: Stator exit plane; **E**: Exit duct/control volume exit plane.

mounted. Instrumentation management and flight hardware are mounted on a central chassis that is 3D printed as one piece for rigidity and to reduce complexity. Cantilevered propulsor arms are attached to the central chassis with a double mortise and tenon style mount, fastened by one M3 cap-head as in Fig. 2. Modularity allows for design iteration and rapid part replacement if required.

The following hardware is mounted directly onto the central chassis:

- **Pixhawk 4 Flight Control hardware** – Packaged, customizable autopilot hardware
- **PM07 Power Module** – Power module managing distribution of power from battery/power supply to flight controllers, other on-board computers, and motors
- **Raspberry Pi 3 Model A+** – On-board computer managing data acquisition and assisting flight controller automation

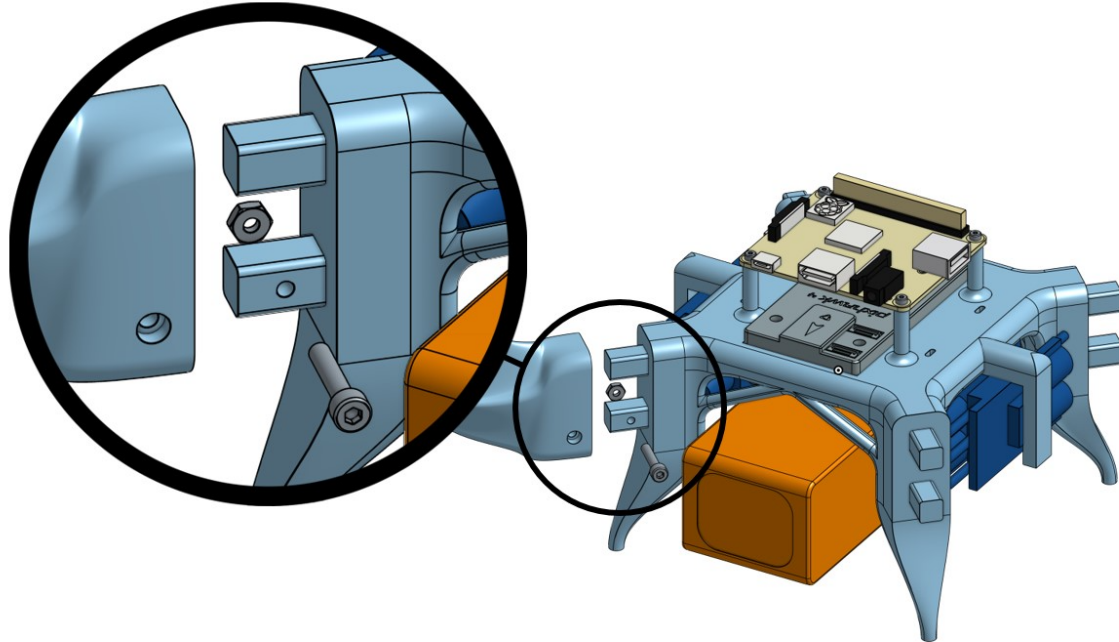


Figure 2: Flying test bed chassis showing exploded detail of double mortise and tenon joint for propulsor arms

- ***ADCPi ADC Breakout*** – Analogue to digital converter mounted directly to the Raspberry Pi 3
- **4x Aerostar 50A ESC** – Electronic Speed Controller driving BLDCM motors
- **Optional: Turnigy 5000mAh 14.8V (4-cell) Battery** – Large capacity 14.8V (nominal) battery. Can be replaced by a tethered 12V power supply.

The central chassis has dimensions of approximately 125mm x 139mm x 93mm (see Fig. 25). It has a dry mass (excluding battery) of 0.529kg and the battery has a mass of 0.466kg.

2.1.2 Customisation of *Pixhawk 4* flight hardware/software

Pixhawk 4 is a packaged flight control hardware system running open source PX4 firmware. Interaction with the system is via the GUI QGroundControl and either a wireless telemetry transmitter-receiver pair or a serial connection (such as a USB). QGroundControl allows a predetermined automated flight path to be followed or alternatively the hardware can be configured to allow manual control provided adequate control inputs can be provided (a 16-channel remote with an 8-channel PPM-PWM converter is used here). The PM4 firmware

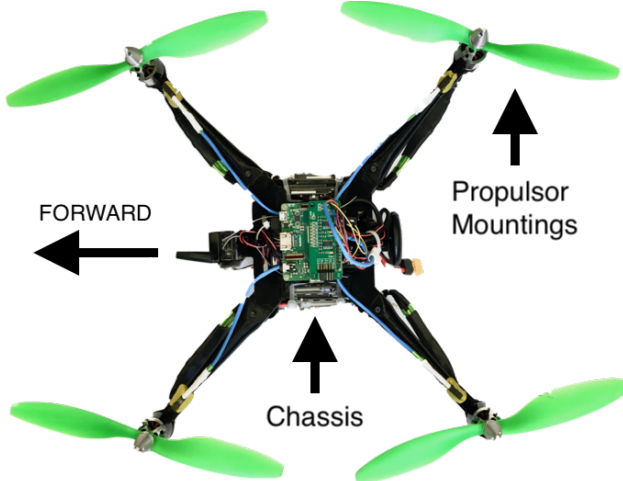


Figure 3: Image of flying test bed with propellers attached

includes various airframe configuration profiles, enabling it to adapt to the vehicle configuration and motor layout. The flying test bed is configured as a symmetric ‘X’ quadcopter. The profile was tuned to the flying test bed by varying PID gains on the control software, ensuring stable operation in hover. It provides a stable hover mode that is intended to reduce horizontal position deviation and maintain a fixed altitude. This means only small corrective inputs are required from the operator to ensure near stationary hover even in enclosed environments. It was found however that wall effects can be significant and so care must be taken when operating in such environments.

2.1.3 Subsystem Functions

Raspberry Pi 3 Model A+ (RPi3)

The RPi3 is a light-weight, small-footprint, 64-bit quad-core processor with UNIX-based operating system and Wi-Fi connectivity that can be run ‘blind’ through an SSH connection from a remote machine. It provides data acquisition and on-board data processing in Python and is used to pre-process test data before wirelessly transferring it back to the remote machine. RPi3 has 28 general purpose input/output (GPIO) pins as well as I²C and serial interfaces among others.

ADCPi ADC Breakout

The ADC breakout board is designed specifically for the RPi3. Operating through the I²C interface, each breakout board provides an 8-channel ADC at 11 to 17 bit resolution with sample rates of 240 to 3.75 *samples/sec* respectively.

PM07 Power Module

Designed to operate in tandem with the Pixhawk 4 flight controller, the PM07 provides power control for all the high-power outputs (such as the motors) as well as a regulated 5V

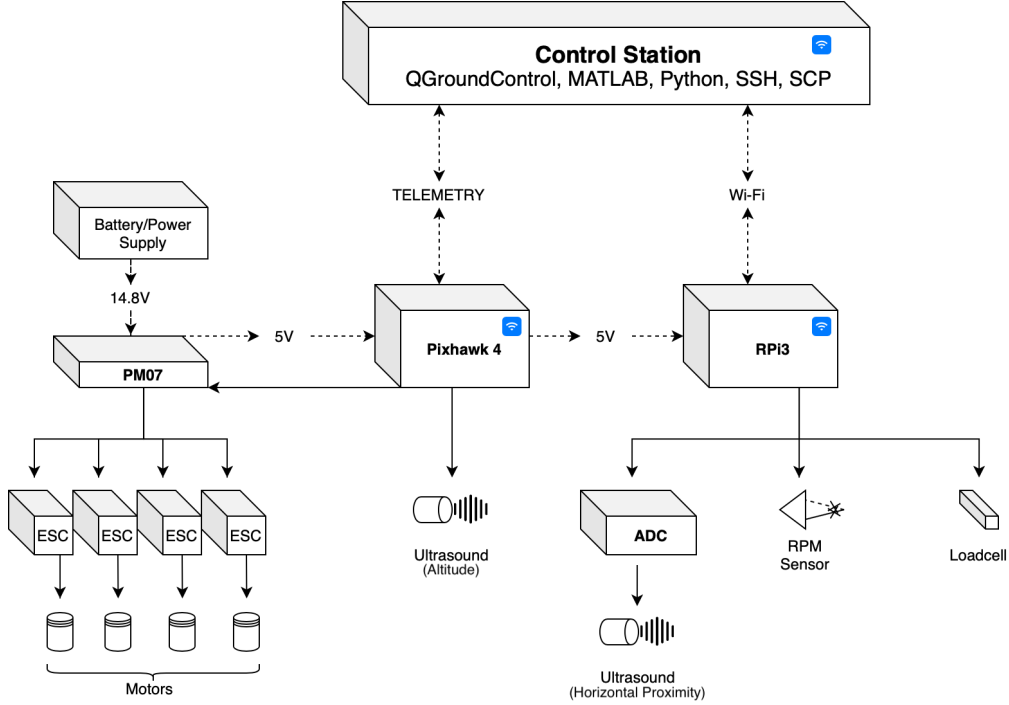


Figure 4: Subsystem schematic of flying test bed

output for the flight controller and RPi3. Power input is 7-51V DC and the output current is limited to 120A (approximately 30A per propulsor). The battery selected can operate up to 125A to accommodate this demand. PM07 also provides 2 ADC inputs.

2.1.4 Subsystem Interaction

Pixhawk 4 provides simple subsystem interaction through its input ports. 5 ports connect the flight controller to the power module: 2x power inputs, 1x motor PWM outputs, 1x auxiliary PWM output, and 1x ADC input. The serial port on the Pixhawk 4 is rewired to connect to the RPi3's UART TXD and RXD terminals (Fig.24 shows all connections made to the RPi3 header). The I²C port connects to an I²C bus that allows up to 5 devices to interface with the Pixhawk 4, including 3 ultrasound sensors measuring proximity in the x, y, and z directions. These sensors can optionally be connected via the ADC for use by the RPi3. Figure 4 shows schematically how the subsystems interact.

2.1.5 Telemetry

Pixhawk 4 wireless telemetry

The plug-and-play telemetry module allows wireless connection to the Pixhawk 4 from a ground control station on a remote machine such as QGroundControl. This is used to communicate with the Pixhawk 4 about flight control and to log power usage data (PM07 voltage and current output).

SSH/SCP on RPi3

RPi3 is wireless enabled allowing it to be accessed remotely via the SSH (secure shell) protocol. SCP (secure copy protocol) allows files to be copied to and from the RPi3. This is used after data collection to collect all data on the remote machine. A dedicated wireless router is used to connect the RPi3 to a remote machine – done automatically on start-up of the RPi3.

Ducted Fan Aerodynamic Design

3.1 Introduction

This section describes the aerodynamic design of an electric ducted fan, 3D printed in PLA, that is designed to replace a propeller on a VTOL electric vehicle. The flying test bed is powered by 4 ducted fans and is required to be able to achieve a steady hover with a payload equal to the weight of the flying test bed. Figure 1 shows a schematic of the ducted fan configuration with labelled blade passage casing radius r_c , blade passage hub radius r_h , diffuser exit casing radius (r_c)_{EXIT}, diffuser exit hub radius (r_h)_{EXIT}, rotor angular velocity Ω , blade passage axial velocity V_x , and diffuser exit velocity V_e . The design process is summarised by the flow chart in Fig. 5. The MATLAB design code developed to design the ducted fan follows the same flow.

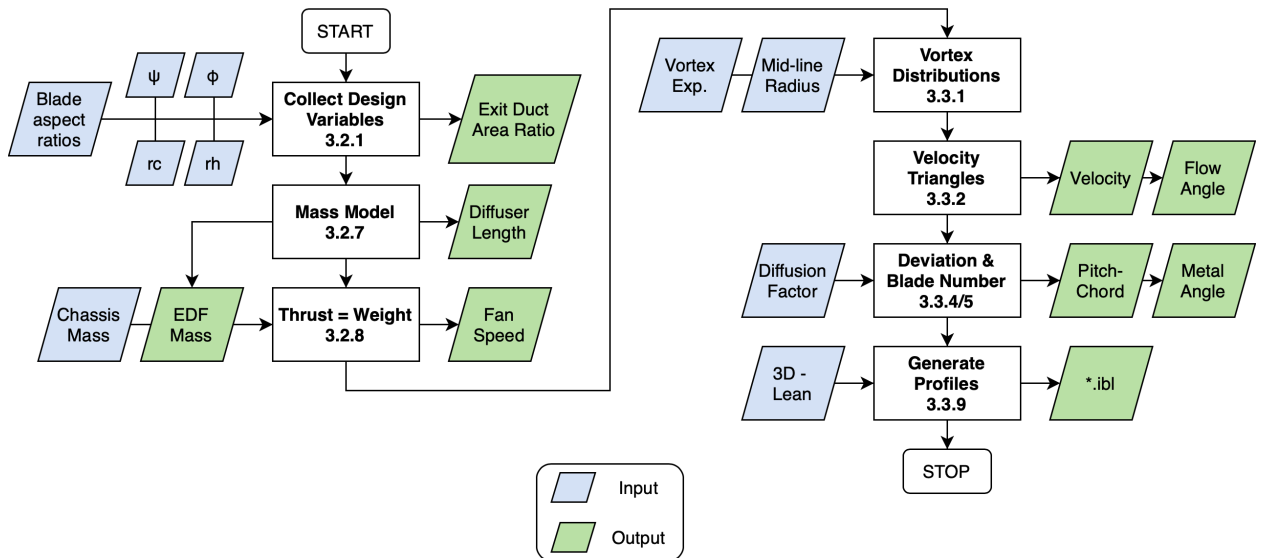


Figure 5: Flow chart showing the aerodynamic design process. 2D design stages are on the left and the 3D design stages are on the right. Processes are labelled by the report section in which they appear (3.#.#)

3.2 Mean-line Design

3.2.1 Non-dimensional Operating Point:

The design of the rotor and stator fan blades is determined by the choice of non-dimensional operating point given by flow coefficient (Eqn. 7a) and stage loading (Eqn. 7b) where the mean-line blade velocity is $U = \Omega \cdot r_m$ with r_m equal to the mean-line radius.

$$\phi = \frac{V_x}{U} \quad (a) \qquad \psi = \frac{\Delta h_0}{U^2} \quad (b) \quad (7)$$

Assuming isentropic flow, stage loading can be written in terms of the stagnation pressure rise, Δp_0 . Using Bernoulli and the assumption exit static pressure is equal to atmospheric gives an expression for Δh_0 in terms of axial blade passage velocity V_x and area ratio.

$$\begin{aligned} \Delta p_0 &= (p_0)_e - (p_0)_{in} = (p_e + \frac{p_a}{2} \rho V_e^2) - p_a \\ \Delta p_0 &= \frac{1}{2} \rho V_e^2 \\ \Delta h_0 &= \frac{\Delta p_0}{\rho} \end{aligned} \quad (8)$$

$$\Delta h_0 = \frac{V_x^2}{2\sigma^2} \qquad \therefore \psi = \frac{V_x^2}{U^2} \cdot \frac{1}{2\sigma^2} \quad (9)$$

Therefore ϕ , ψ , and σ are related by

$$\psi = \frac{\phi^2}{2\sigma^2} \quad (10)$$

The operating point can therefore be defined by the area ratio, σ and the flow coefficient, ϕ . This allows the desired figure of merit to be chosen and the required stage loading to be found.

3.2.2 Fan Operating Speed:

Equation 6 shows that the figure of merit for a ducted fan in hover is independent of the speed of rotation of the fan. The fan speed, however, impacts the magnitude of thrust developed, shown by substituting Eqn. 7(a) into Eqn. 4.

$$T = \frac{\rho A_x (\Omega r_m \phi_m)^2}{\sigma} \quad (11)$$

This shows thrust to vary with both fan speed and fan size, and so the required thrust will vary depending on the choice of these parameters. The effect of fan size is discussed in section 3.2.

3.2.3 Mean-line Location:

Maximising the flow area for a given propulsor radius maximises thrust developed (Eqn. 11) and ensures minimum use of material and therefore a lighter design. This results in a small hub radius (limited only by electric motor size, typically $\approx 20\text{mm}$) and consequently low hub-to-tip ratios (< 0.5). Selecting a mean-line at the midspan radius gives different mass flows above and below the mean-line and this results in variation in loading across the span. An alternative mean-line position is defined by balancing the mass flow above and below the mean-line. This sets the mean-line radius at the root-mean-square of the hub and tip radii

$$r_m = \sqrt{\frac{r_h^2 + r_c^2}{2}} \quad (12)$$

3.2.4 Overall Performance

The expressions for fan thrust and power can now be determined in terms of the non-dimensional operating point and the fan's geometric variables tabulated in Table 1.

$$T = \frac{\rho\pi\phi_m^2\Omega^2(r_c^4 - r_h^4)}{2\sigma} \quad (13)$$

$$P = \frac{\rho\pi\phi_m^3\Omega^3(r_c^2 - r_h^2)}{2\sigma^2} \left(\frac{r_c^2 + r_h^2}{2} \right)^{\frac{3}{2}} \quad (14)$$

r_c	Blade passage casing radius
r_h	Blade passage hub radius
L	Length of propulsor intake and blade passage
Ω	Rotor angular velocity
σ	Diffusion factor
ϕ_m	Mean-line flow coefficient
ψ_m	Mean-line stage loading

Table 1: Variables defining propulsor performance

3.2.5 Design Objectives and Constraints

Equation 6 shows the design objective to be to maximise the exit duct area ratio. Area ratios of $\sigma > 1$ require the exit duct to diffuse the flow introducing an adverse pressure gradient and requiring the duct to increase in length to avoid separation. Therefore there is a trade-off between propulsor figure of merit and propulsor length and weight. Using a scaling argument, the weight of the propulsor can be shown to scale with σ^2 , compared to figure of merit which scales with $\sigma^{0.5}$ as in eqn. 6. Power must be minimised for a given payload

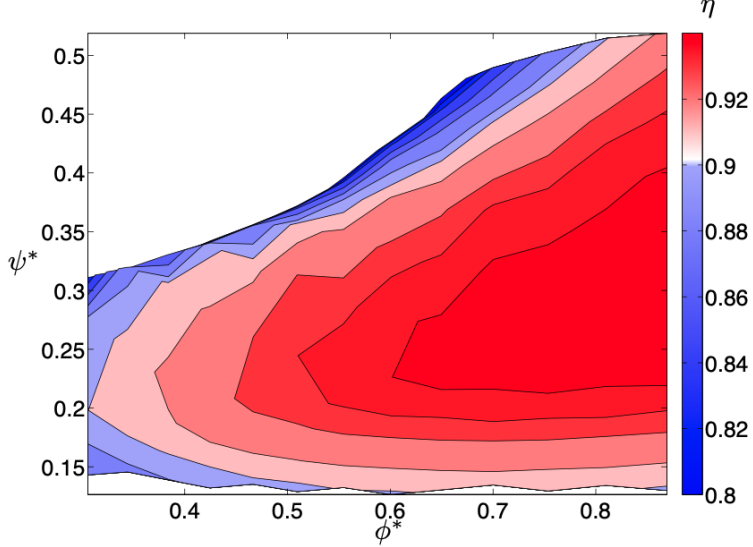


Figure 6: Rotor efficiency η at design incidence $i = -3^\circ$ as a function of flow coefficient and stage loading coefficient (reproduced from Maffioli (2015))

thrust and so this sets a constraint on the size of the diffuser. A mass model is required to couple the fan performance to the diffuser size and total vehicle weight to quantify the limit on fan size.

Blade efficiency at low Reynolds numbers also constrains the design space. Maffioli (2015)[1] determined a low Reynolds number Smith chart for the blade profiles used here which is presented in Fig. 6. It shows blade efficiency in a 2D cascade to decrease for flow coefficients $\phi_m < 0.6$ and stage loading $\psi_m < 0.2$. This is verified by Corralejo and Harley (2017)[2]. Maffioli defines blade efficiency in terms of upstream and downstream stagnation temperature and pressure by

$$\eta = \frac{T_{02s} - T_{01}}{T_{02} - T_{01}} = \frac{\left(\frac{P_{02}}{P_{01}}\right)^{\gamma-1/\gamma} - 1}{\frac{T_{02}}{T_{01}} - 1} \quad (15)$$

3.2.6 ESDU 75026 Diffuser Data:

ESDU 75026 ‘*Static-pressure recovery coefficient, symmetrical annular diffusers without tailpipes*’[3] presents the performance of symmetric annular diffusers in incompressible flow. The length of diffuser required to prevent separation is estimated from Fig. 7 which gives empirical limits of separation at various diffuser lengths and area ratios for symmetric annular diffusers. Considering Eqn. 3 and Bernoulli, static pressure recovery can be written as

$$C_{pr} = \frac{p_e - p_x}{\frac{1}{2}\rho V_x^2} = 1 - \frac{1}{\sigma^2} \quad (16)$$

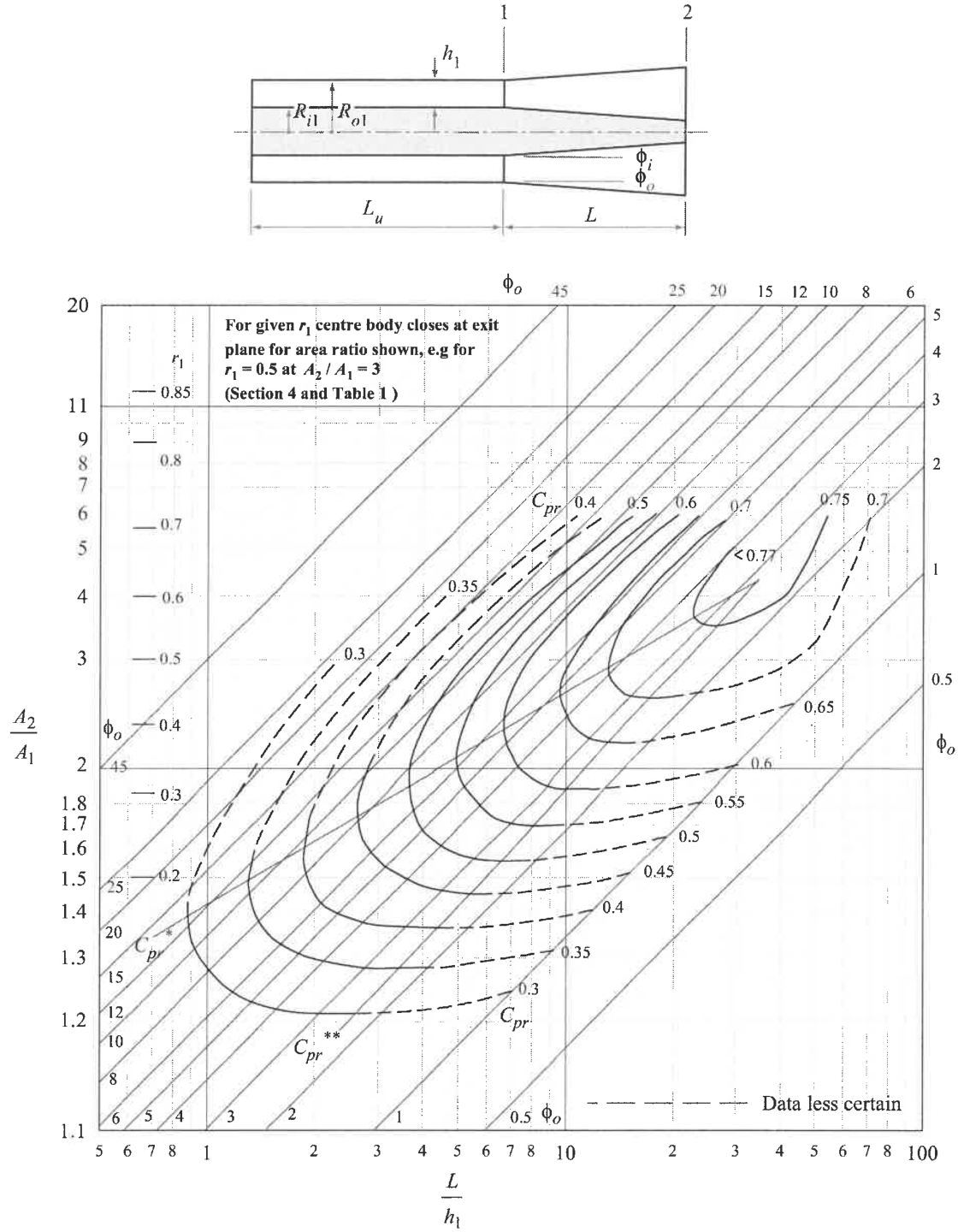


Figure 7: Static-pressure recovery coefficient, symmetrical annular diffusers without tailpipes and with fully developed entry flow, $L_u/h_1 \geq 100$

Figure 7 shows two limit lines, C_{pr}^* and C_{pr}^{**} representing the separation limit and the limit of performance due to frictional loss and boundary layer growth respectively. Designing on the appropriate constant C_{pr} line close to C_{pr}^{**} will produce a diffuser that is unlikely to detach. This line can be approximated with an R-squared value of 0.9999 by

$$\frac{L}{r_c - r_h} = -5.56\sigma^3 + 24.16\sigma^2 - 23.41\sigma + 5.413 \quad (17)$$

3.2.7 Mass Model

Figure 8 shows an exploded view of the components making up the mass model of the ducted fan. The diffuser hub and casing, and the intake are modelled as hollow truncated cones. The blade duct hub and casing are modelled as hollow cylinders. Blade rows are modelled as thin annular disks.

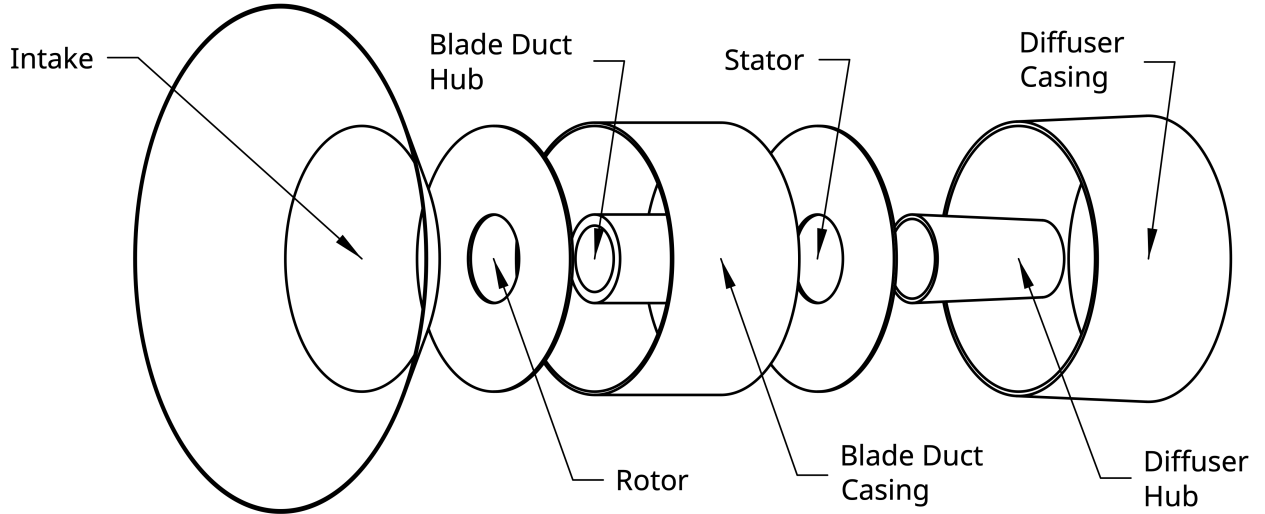


Figure 8: Exploded view of ducted fan mass model components

Diffuser: The diffuser hub and casing are modelled as a hollow truncated cone with height L_{DIFF} (determined by Eqn. 17), a base radius r_h (for the hub) and $(r_c)_{EXIT}$ (for the casing), a truncation radius of $(r_h)_{EXIT}$ (for the hub) and r_c for the casing, and a thickness t , as in Fig. 1. Equation 18 gives the volume of a hollow truncated cone with the respective values of R , r , S , and s for the hub and casing defined in tab. 2.

$$V = \frac{h\pi}{3}(R^2 + Rr + r^2 - S^2 - Ss - s^2) \quad (18)$$

$$m_{DIFF} = \rho_{PLA}(V_{HUB} + V_{CASE}) \quad (19)$$

From the ESDU data, a annulus flow with uniform axial velocity is diffused in the shortest distance if the diffuser is symmetric such that the diffuser angle at casing and hub is equal giving

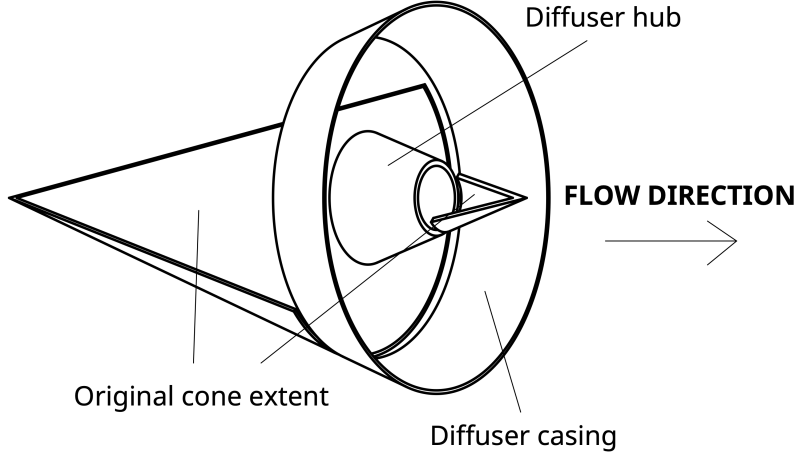


Figure 9: Hollow truncated cone diffuser model showing original extent of cone before truncation

$$\frac{(r_c)_{EXIT} - r_c}{L} = \frac{r_h - (r_h)_{EXIT}}{L} \quad (20)$$

Applying Eqn. 20 and expanding Eqn. 2 in terms of radius, the diffuser exit hub and casing radii can be determined.

$$(r_h)_{EXIT} = \frac{r_c + r_h}{2} - \frac{\sigma}{2}(r_c - r_h) \quad (21)$$

$$(r_c)_{EXIT} = \frac{r_c + r_h}{2} + \frac{\sigma}{2}(r_c - r_h) \quad (22)$$

Substituting Eqn. 21 and Eqn. 22 into Eqn. 18, Eqn. 19 can be solved to approximate the mass and therefore the weight of a diffuser at a particular set of design parameters.

Blade Passage: The blade passage (excluding rotor and stator) are modelled as a straight annulus 3D printed in PLA. The passage itself has inner radius r_h and outer radius r_c . The casing is modelled to have thickness of $t_c = 1.5\text{mm}$ and the hub section has a thickness of $t_h = 5\text{mm}$. The length of the blade passage is $L_{BP} = 70\text{mm}$ giving a volume of

$$V_{BP} = L_{BP}\pi[2r_h t_h - t_h^2 + 2r_c t_c + t_c^2] \quad (23)$$

Multiplying by the density of PLA gives the mass of the blade passage section, which can be written in terms of the unknown variable r_c and r_h

$$m_{BP} = 2.73r_h + 0.818r_c - 0.0062 \quad (24)$$

	Hub value	Casing value
R	r_h	$(r_c)_{EXIT} + t$
r	$(r_h)_{EXIT}$	$r_c + t$
S	$r_h - t$	$(r_c)_{EXIT}$
s	$(r_h)_{EXIT} - t$	r_c
h	L	L

Table 2: Parameter values for diffuser hub and casing

Intake: For simplicity the intake is also modelled as a hollow truncated cone, an approximation for it's actual ellipsoidal geometry. It has approximately equal length to it's change in radius which is set approximately equal to the blade passage span, $r_c - r_h$. Therefore using Eqn. 18, and assuming a thickness of 1mm, the intake mass can be approximated by

$$m_{IN.} = 3.90(r_c - r_h)(3r_c - r_h + 0.001) \quad (25)$$

Blades: As the number of blades has not yet been determined, the blades are modelled as having the equivalent mass of a annular flat disk of thickness $t_{ROTOR} = 1.5mm$ for the rotor and $t_{STATOR} = 1.5mm$ for the stator. The resulting mass is given by

$$m_{BLADES} = \rho_{PLA}\pi(r_c^2 - r_h^2)(t_{ROTOR} + t_{STATOR}) \quad (26)$$

$$m_{BLADES} = 11.7(r_c^2 - r_h^2) \quad (27)$$

Thrust–Weight Balance: The mass model described above provides an approximation for the mass of a particular design based on the design parameters listed in tab. 1. In hover, the load carried by each propulsor is equal to the propulsor's weight and its share of the payload weight (4 propulsors). The payload here is the flying test bed chassis and battery, described in section 2.1. Using Eqn. 13 the thrust developed can be set equal to the required thrust to give the relationship between the design variables when the propulsor is operating in the static hover state.

$$T = g \left[m_{PROPSOR} + \frac{m_{CHASSIS}}{4} + \frac{m_{BATTERY}}{4} \right] \quad (28)$$

$$\frac{\rho\pi\phi_m^2\Omega^2(r_c^4 - r_h^4)}{2\sigma} = g[m_{DIFF.} + m_{BP} + m_{IN.} + m_{BLADES}] + 2.44N \quad (29)$$

3.2.8 Design Selection

In order to solve the design problem, the number of unknowns must be reduced. This is achieved by fixing the propulsor size. The application demonstrated here is for a small quadcopter style vehicle. Furthering work carried out by Barry (2019)[4] in which the performance of a ducted fan was determined with $M_F > 1$ and $r_c = 120mm$, this design is to be scaled by a half giving

$$r_c = 60mm \quad (30)$$

The value of r_h is determined by the outer diameter of the electric motor used to drive the rotor. This is typically $d < 35mm$, therefore r_h is chosen to be

$$r_h = 20mm \quad (31)$$

Giving a hub-to-tip ratio of 0.333. This leaves area ratio, σ , and the rotor angular velocity, Ω . The relationship between the design parameters ϕ , ψ , and σ , as well as the relationship between diffuser length and σ , results in a limit on the design point due to the requirement for diffuser length, $L_{DIFF.}$, to not become prohibitive (as discussed in sec. 3.2: *Overall Performance*). This is limited to $L_{DIFF.} \leq 100mm$. Therefore from Eqn. 17

$$-5.56\sigma^3 + 24.16\sigma^2 - 23.41\sigma + 5.413 \leq 2.5 \quad (32)$$

$$\therefore \sigma \leq 1.2 \quad (33)$$

It should be noted that this limit on σ arises from the performance of a conventional symmetric annular diffuser, as presented in ESDU 75026. This limit may be exceeded however through the use of various flow devices, such as splitter vanes. These ideas are discussed further in the future work section (Section 7) and are not implemented here. With the other parameters set, the thrust = weight condition sets the value of Ω at each design point. The required motor speed impacts the choice of electric motor used as the maximum efficiency range will vary.

Figure 10a shows the variation in figure of merit across the design space. The diffuser length limit considerably constrains what sections of the design space are accessible, regardless the majority of the design space provides significantly better hover performance than a propeller. Figure 10b shows the variation in required motor speed (in RPM) across the design space. The required optimum efficiency range for the electric motor must be between 5,500 – 14,000 RPM. In order to reduce motor size the lower end of this range is chosen

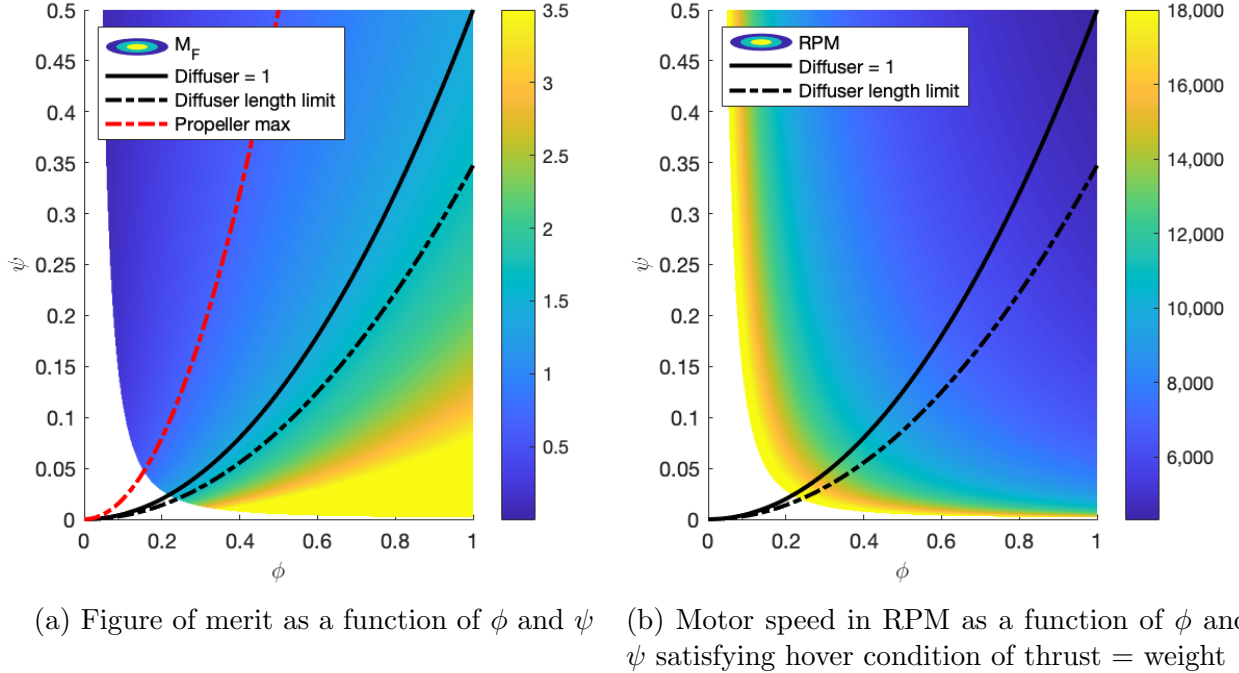


Figure 10: Contour plots of the ϕ - ψ design space generated using mass model. Plots display the diffuser limit arising from a maximum diffuser length, and the line representing a area ratio of 1.

(this is discussed in more detail in Section 4) therefore $\Omega \sim 6500$ RPM. SOMEONE 20XX³ shows suitable range for flow coefficient in incompressible turbomachinery to not exceed 0.8, and stage loading to not exceed 0.3. Considering Fig. 10b a line of constant RPM at approximately 6500 RPM in the region between the two diffuser limits passes from top-left to bottom-right. Figure 10a shows figure of merit to increase towards the bottom-right and so to satisfy all the conditions above and maximise figure of merit, an operating point is chosen with $\phi_m = 0.8$ and $\psi_m = 0.25$ and is tabulated in Table 3.

Conventional propulsive turbomachines, such as high bypass ratio turbo-fans must limit their flow coefficient as this comes at the cost of propulsive efficiency. The propulsor considered here however differs from this as it diffuses the exit flow, reducing its velocity and therefore reducing exit loss.

Velocity Triangles: Now the design parameters have been determined the mean-line velocity triangles can be drawn for this particular design.⁴ Figure 11 shows the velocity triangles in context with rotor and stator blades. Flow angles are measured positive in the sense of rotor rotation (in Fig. 11 positive down).

³REFERENCE SMITH CHARTS? LOOK AT WHY LIMITING PSI AND PHI

⁴PUT DERIVATION OF TRIANGLE ANGLES IN APPENDIX?

r_c	60mm
r_h	20mm
r_m	44.7mm (RMS)
Ω	6230 RPM
σ	1.1314
$L_{DIFF.}$	72.0mm
ϕ_m	0.80
ψ_m	0.25

Table 3: Propulsor design point

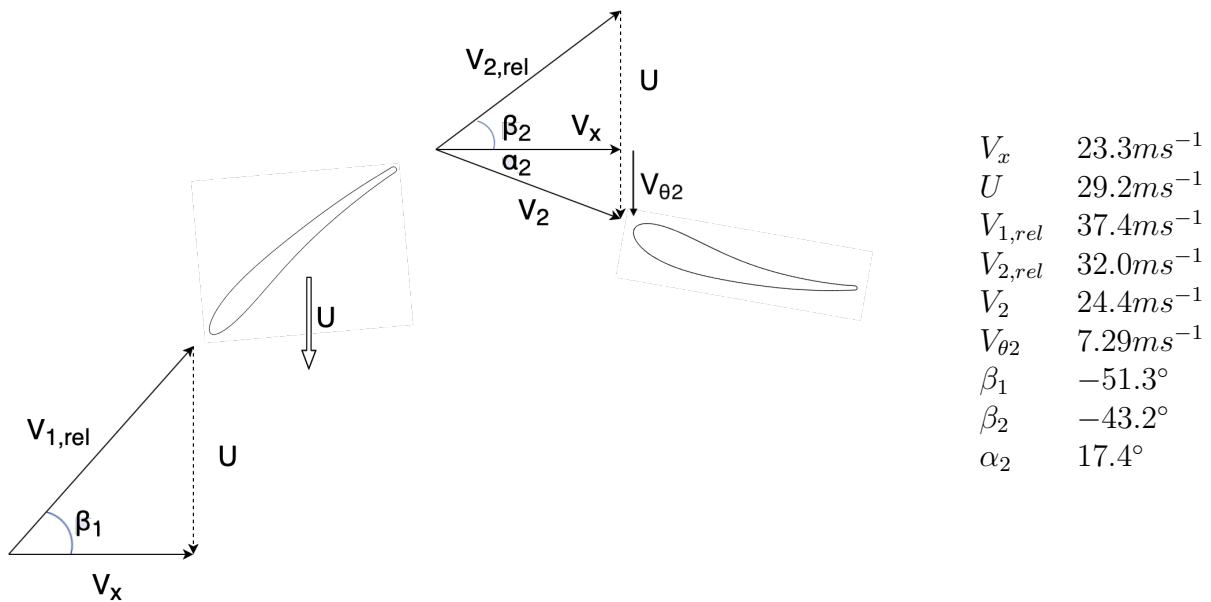


Figure 11: Mean-line velocity triangles (stator exit omitted as flow axial at exit)

3.3 3D Blade Design

Overall performance has been determined by setting the mean-line values of flow coefficient, ϕ_m , and stage loading, ψ_m . The values of ϕ and ψ must vary along the span as the local value of blade speed changes, and for equilibrium to be maintained across the flow passage. In order to satisfy these conditions the radial equilibrium equation must be satisfied. Potential solutions to this equation are discussed below.

3.3.1 3-dimensional Flow Solutions to Radial Equilibrium:

Radial equilibrium states that for axi-symmetric and incompressible annulus flow Eqn. 34 must be satisfied.

$$\frac{dh_0}{dr} - T \frac{ds}{dr} = V_x \frac{dV_x}{dr} + \frac{V_\theta}{r} \frac{d(rV_\theta)}{dr} \quad (34)$$

Assuming there is no variation in stagnation enthalpy or entropy across the span, this reduces to

$$V_x \frac{dV_x}{dr} + \frac{V_\theta}{r} \frac{d(rV_\theta)}{dr} = 0 \quad (35)$$

Noting Eqn. 7 and applying Euler's work equation, we obtain

$$\phi r \frac{d(\phi r)}{dr} + \psi \frac{d(\psi r^2)}{dr} = 0 \quad (36)$$

Which has general solutions in the form

$$\phi = \phi_m \left(\frac{r}{r_m} \right)^A \quad (a) \qquad \psi = \psi_m \left(\frac{r}{r_m} \right)^B \quad (b) \quad (37)$$

Where ϕ_m and ψ_m are the mean-line quantities. Substituting eqns.37a & 37b into Eqn. 36 gives⁵

$$\begin{aligned} \left[\phi_m \left(\frac{r}{r_m} \right)^A \right]^2 (1 + A) &= - \left[\psi_m \left(\frac{r}{r_m} \right)^B \right]^2 (2 + B) \\ \therefore \phi^2 (1 + A) &= -\psi^2 (2 + B) \end{aligned} \quad (38)$$

This solution can be used to determine the values of the exponents, A and B . The constant B is referred to here as the vortex distribution exponent as it determines the tangential velocity variation in the r - θ plane.

Free Vortex ($B = -2$): One such distribution arises from the free vortex condition. This results from the solution to Eqn. 38 in which both LHS and RHS are equal to zero giving

$$A = -1 \quad (a) \qquad B = -2 \quad (b) \quad (39)$$

Therefore from Eqn. 37a and Eqn. 39a

$$\phi(r) \sim \frac{1}{r} \qquad \therefore \frac{d}{dr}(V_x) = 0 \quad (40)$$

Therefore axial velocity across the span must be constant. Similarly it can be shown from Eqn. 37b and Eqn. 39b

$$\psi(r) \sim \frac{1}{r^2} \qquad \therefore \frac{d}{dr}(\Delta h_0) = 0 \quad (41)$$

⁵STICK THE DERIVATION IN AN APPENDIX????

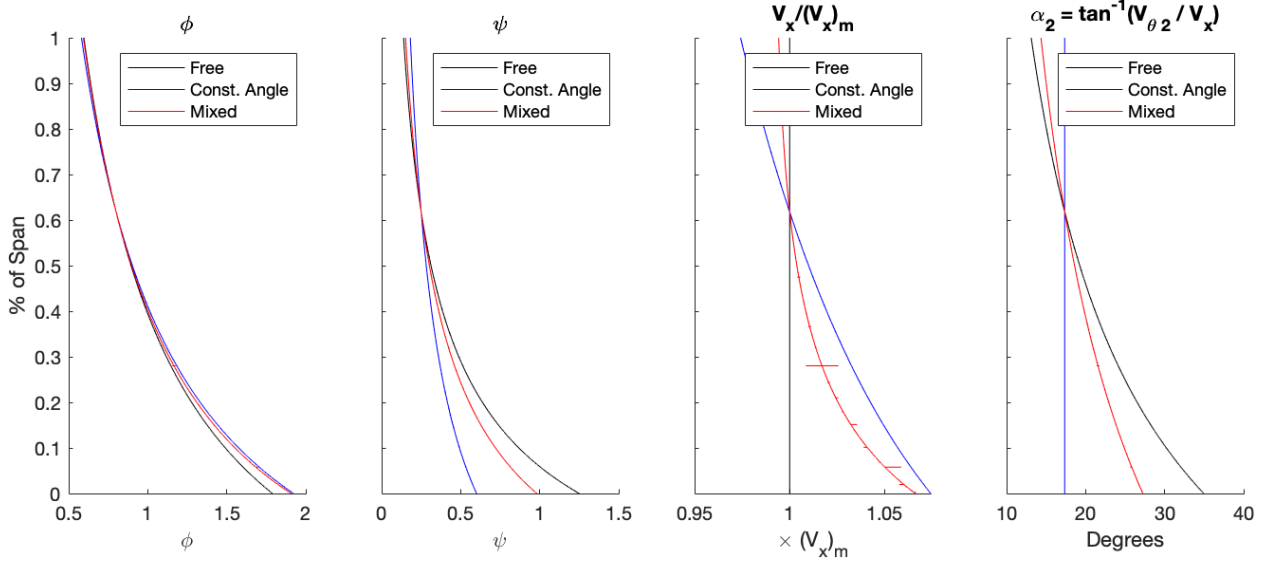


Figure 12: Distributions of design parameters ϕ and ψ and non-dimensionalised axial and tangential velocities, V_x and $V_{\theta 2}$ respectively, across the span at 3 different boundary conditions (free vortex, constant angle and mixed vortex).

Therefore the loading is equal across the span. It can then be determined that $V_{\theta 2} \sim 1/r$ resulting in a vorticity free (lowest loss) flow[5]. Both the constant V_x and the constant Δh_0 conditions indicate uniform exit static pressure. In practice the variation in $V_{\theta 2}$ across the span results in large variations in blade twist angle that can reduce efficiency (see Fig. 12 that shows $V_{\theta 2}$ variation resulting in over 20° of absolute flow angle variation).⁶

Furthermore, Fig. 12 shows stage loading, ψ , to become larger than 1 at radii close to the hub. From Euler, and given axial inlet flow

$$\Delta V_\theta = V_{\theta 2} = \psi U \quad (42)$$

This shows the tangential velocity at the hub to be greater than the local blade speed. By reducing the value of the vortex distribution exponent, B , this can be avoided by keeping $\psi_{HUB} \leq 1$.

Mixed Vortex ($-2 \leq B \leq 0$): Equation 38 can also be used to numerically solve the radial equilibrium equation for any value of the vortex distribution exponent provided ϕ_m and ψ_m are known. A summary of vortex distribution exponent values is shown in tab. 4. The mixed vortex design shown in Fig. 12 has a vortex distribution exponent of -1.7 . This produces a vortex distribution that, at the hub, has a tangential velocity is equal to the velocity of the hub wall. This reduces the absolute velocity of the flow past the wall and therefore minimises frictional loss at the hub. Hereafter any reference to a ‘mixed vortex condition’ corresponds to a vortex distribution exponent of $B = -1.7$, as described here.

⁶AGAIN NEED A REFERENCE FOR THIS?

Constant Angle: Another common design is for constant absolute flow angle across the span, such that

$$\frac{d}{dr} \left(\frac{V_\theta}{V_x} \right) = 0 \quad (43)$$

$$\therefore \frac{\psi}{\phi} = \text{constant} \left(= \frac{\psi_m}{\phi_m} \right) \quad (44)$$

This results in the exponents A and B being equal giving

$$A = B = - \left(\frac{2\psi_m^2 + \phi_m^2}{\psi_m^2 + \phi_m^2} \right) \quad (45)$$

Free Vortex	Constant Angle	$B = \dots$
$V_x(r) = \text{const.}$	$V_x/V_\theta = \text{const.}$	see Eqn. 38

A	-1	$-\left(\frac{2\psi_m^2 + \phi_m^2}{\psi_m^2 + \phi_m^2}\right)$	<i>Solve numerically</i>
B	-2	$-\left(\frac{2\psi_m^2 + \phi_m^2}{\psi_m^2 + \phi_m^2}\right)$	<i>Solve numerically</i>

Table 4: Vortex distribution exponents for various boundary conditions

3.3.2 3D Velocity Triangles:

Once the distributions of ϕ and ψ have been determined the variation in flow velocities and angles can be found across the span. The value of any velocity or angle can be found using the appropriate local values of the spanwise variables ϕ , ψ , U , and r . The relative merits of each of the vortex distributions are discussed in Section 6.1.1 in which the three designs presented here are tested.

3.3.3 Validation of Mean-line Location:

Eqn. 13 and Eqn. 14 come from the assumption that mean-line design parameters are representative of the performance of the whole flow. This assumption can be verified now that

the span-wise distribution of the flow parameters has been determined. Integrating the work done and thrust generated by an infinitesimal annulus element allows the real power and thrust produced by the propulsor to be determined. This is computed numerically and the expression obtained above for each of the parameters in Eqn. 48.

$$P = \int_{r_h}^{r_c} \Delta h_0 \cdot d\dot{m} \quad (46)$$

$$\Delta h_0 = \psi U^2 \quad (a) \quad d\dot{m} = \rho V_x (2\pi r dr) \quad (b) \quad (47)$$

$$\therefore P = 2\pi\rho\Omega^3 \cdot \frac{\phi_m \psi_m}{r_m^{B+A}} \int_{r_h}^{r_c} r^{A+B+3} dr \quad (48)$$

A similar expression can be obtained for the thrust developed. The mass-averaged mean-line radius definition of r_m is compared to the conventional mean-line radius definition of r_m in Table 5 by calculating the error between the real power and thrust and the predicted one obtained from Eqn. 14 and Eqn. 13. A properly balanced mean-line radius choice will ensure the real power is as close to the predicted one as possible, minimising this error

Mean-line radius	P error	T error
$r_m = \text{mean}(r_c, r_h)$	37%	24%
$r_m = RMS(r_c, r_h)$	1.2%	0.36%

Table 5: Comparison of power requirement from predicted (from constant mean-line parameters) and real (from integral of span-wise distributions) using various mean-line locations. A mixed vortex design is used though the behaviour is also displayed in other all other vortex designs

Table 5 shows the selection of a mean-line radius at the RMS of the hub and casing radius reduces the error between the real and the predicted power requirements to $\approx 1\%$. These errors are small enough to be neglected and so this choice of mean-line radius is validated.

3.3.4 Blade Number and Span-wise Chord:

Lieblein, Schwenk and Broderick (1953)[6] present a correlation for diffusion factor as a function of velocities and the pitch-chord ratio of the blades.

$$DF = \left(1 - \frac{V_{2,rel}}{V_{1,rel}}\right) + \left(\frac{V_{\theta 1,rel} - V_{\theta 2,rel}}{2V_{1,rel}}\right) \frac{s}{c} \quad (49)$$

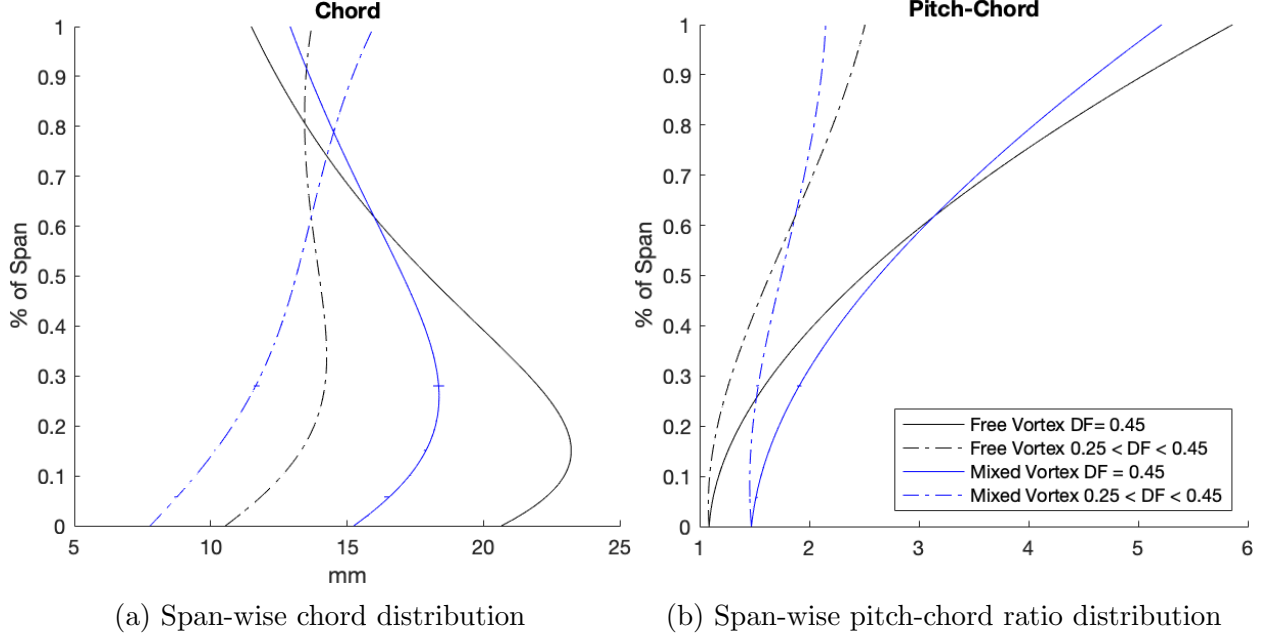


Figure 13: Span-wise distributions are shown for both the free and mixed vortex conditions (black and blue lines respectively). Each is also shown with a constant value of diffusion factor ($DF = 0.45$, solid line) and varying diffusion factor linearly across the span ($DF_{HUB} = 0.45$; $DF_{TIP} = 0.25$, dot-dashed line)

Given that the change in tangential flow velocity is the same in both the absolute and the rotor relative reference frames, and the inlet flow is axial, this becomes

$$DF = \left(1 - \frac{V_{2,rel}}{V_{1,rel}}\right) + \left(\frac{V_{\theta 2}}{2V_{1,rel}}\right) \frac{s}{c} \quad (50)$$

This expression is valid for both the rotor and stator provided the relative values are taken in the respective blade's frame off reference.

Having determined the span-wise variation in the flow velocities and angles in Section 3D Velocity Triangle above, the value of the local pitch-chord ratio, s/c , can be found provided a suitable diffusion factor is chosen. Consider first a constant value of diffusion factor that lies below the separation limit suggested in CUED Turbomachinery I⁷ as $DF_{lim} = 0.6$, such as $DF = 0.45$. Pitch-chord across the span can be determined as

$$\frac{s}{c} = \left[DF - \left(1 - \frac{V_{2,rel}}{V_{1,rel}}\right)\right] \left(\frac{2V_{1,rel}}{V_{\theta 2}}\right) \quad (51)$$

In order to determine span-wise pitch, the number of blades are determined using the mean-line values. The mean-line chord is estimated using the blade mean-line aspect ratio where $AR = \text{span}/\text{chord} = l/c$

⁷reference handout

$$c_m = \frac{r_c - r_h}{AR} \quad (52)$$

$$N = \frac{2\pi r_m}{(s/c)_m c_m} \quad (53)$$

The blade number is rounded up to the next integer value. Table 6 at the end of this section (*Blade Number and Span-wise Chord*) outlines the calculated and selected blade numbers for each of the designs discussed. Using the blade number the local chord can be determined using local pitch-chord ratio and radius such that

$$c = \frac{2\pi r}{(s/c)N} \quad (54)$$

The resulting span-wise chord distribution from both the free and mixed vortex conditions are shown in Fig. 13a (solid line). For the free vortex condition it shows the variation in chord across the span to be large with the tip chord is less than half the maximum chord. Changing to the mixed vortex condition reduces this variation significantly with both the tip chord increasing and the hub chord decreasing. The variation in the free vortex design arises from Eqn. 51 as the range of velocities across the span result in large variations in pitch-chord ratio (as in Fig. 13b).

Vortex Design	Diffusion Factor	N_R	Selected	N_S	Selected
Free Vortex	$DF = 0.45$	(5.60)	6	(4.66)	5
	$0.25 \leq DF \leq 0.4$	(10.48)	11	(7.20)	7
Mixed Vortex	$DF = 0.45$	(5.60)	6	(4.66)	5
	$0.25 \leq DF \leq 0.4$	(10.48)	11	(7.20)	7

Table 6: Rotor and stator blade numbers at various design conditions

Lieblein (1953)[6] shows the increase in loss for diffusion factors above 0.55 in the hub to mean-line regions, and 0.3 in the tip region. Therefore varying the diffusion factor across the span reduces the losses due to high diffusion factor and maintains a constant margin to Lieblein's suggested limits. The dot-dashed lines in Fig. 13b show the same operating point

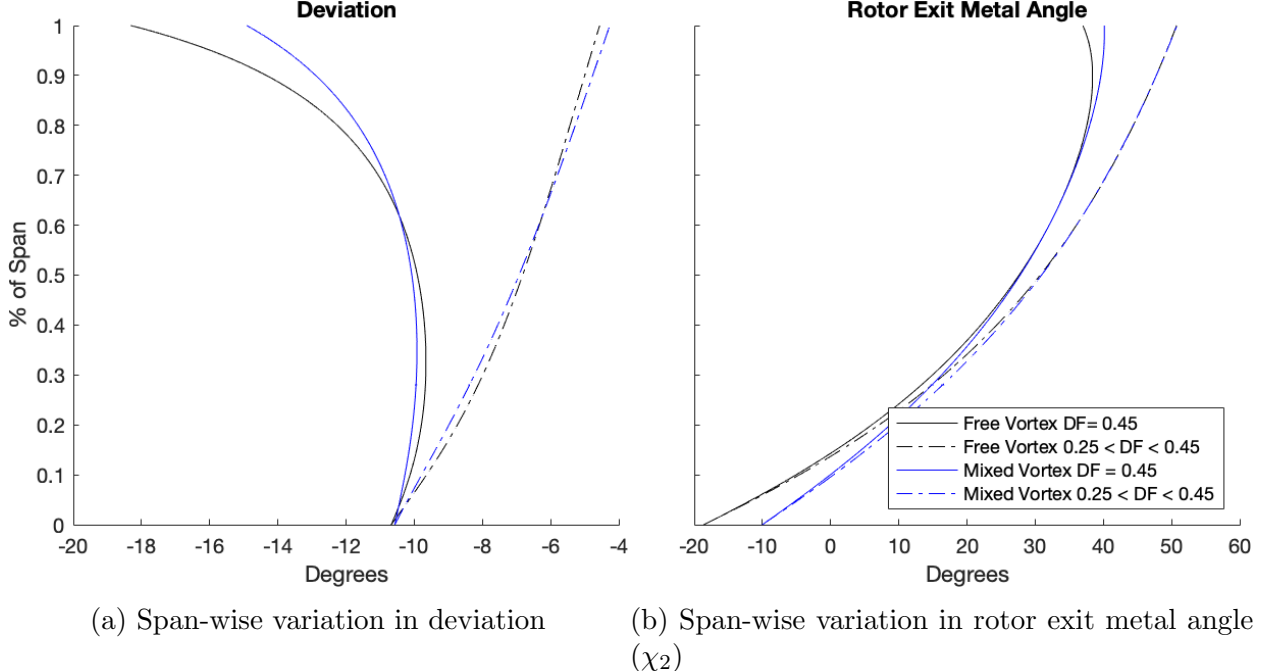


Figure 14: Span-wise distributions are shown for both the free and mixed vortex conditions (black and blue lines respectively). Each is also shown with a constant value of diffusion factor ($DF = 0.45$, solid line) and varying diffusion factor linearly across the span ($DF_{HUB} = 0.4$; $DF_{TIP} = 0.25$, dot-dashed line)

as the solid lines but with the diffusion factor varying linearly from 0.4 at the hub to 0.25 at the tip. This limits the variation in pitch-chord ratio across the span.

Consistency in pitch-chord has further implications for deviation and is explored in the following section.

3.3.5 Deviation

Flow deviation is estimated from correlations proposed by Howell (1945)[7], (1945)[8], and Carter (1950)[9]. Commonly referred to as Carter's rule it states that for a compressor blade

$$\delta = m\theta \sqrt{\frac{s}{c}} \quad (55)$$

Where θ is the flow turning achieved in the relative frame, and m is an empirically determined variable that can be approximated by

$$m = 0.23 \left(\frac{2a}{l} \right)^2 + \frac{\beta_2}{500} \quad (56)$$

Where for a circular arc camber line $a/l = 0.5$. Hence the deviation varies $\sim \sqrt{s/c}$. Figure 14a shows the large increase in deviation angle at the rotor tips for both the free and the mixed vortex conditions when a constant diffusion factor is used (solid lines). Introducing a varying diffusion factor (dot-dashed lines) across the span reduces this deviation as the pitch-chord ratio has varies less across the span (Fig. 13b). Carter's rule is derived from empirical results obtained from compressor cascades (hub-tip ratio ≈ 1), and as such it is not suitable to apply it to blades with large span-wise variations in pitch-chord ratio. By applying a varying diffusion factor the range of pitch-chord ratio reduces significantly and Carter's rule produces more reliable results. Consequently the variation in rotor exit metal angle is more consistent and contains no mid-span maxima, as in Fig. 14b.

3.3.6 Blade Lean

Taylor (2016)[10] shows the limits of using a 2-dimensional design with respect to 3-dimensional flow. Ensuring the blade suction surface subtends the hub and casing at an obtuse angle helps reduce corner separations and trailing edge losses. Lean is added to the rotor and stator blades to satisfy this requirement as in Fig. 15: the rotor has 10° of lean at the hub and approximately 40° at the tip; the stator follows a parabolic lean profile with 10° of lean at the hub and tip.

3.3.7 Noise

Similar blade numbers in the rotor and stator or low common multiples of blade number will result in more blade interaction and therefore higher acoustic dB. If possible, odd or prime numbers are selected to minimise interaction, provided this number is not too far from the calculated value. Table 6 shows the number of blades calculated for each design and the number of blades selected.

3.3.8 Blade Profiles

Low Reynolds number blade profiles were obtained from Maffioli (2015)[1]. Profiles

- Where did they come from?
- What are they?
- How are they implemented?

3.3.9 Design Selection

Figure 5 shows a flowchart for the MATLAB design code developed to produce blade profiles as `*.ibl` files that can be imported into a CAD package to begin the rotor mechanical design.



Figure 15: Perspective render of 3D blade design

Electrical and Mechanical Design

4.1 Introduction

With the propulsor design specified the electrical design must be considered to provide the correct power to drive the propulsors. The electric motor and corresponding power supply is chosen to be compatible with both the propulsor aerodynamic design and the system control and instrumentation architecture.

4.2 Electrical Design

4.2.1 Motor Requirements

In Section 3.2 the motor speed and design point is set. Required motor speed is found to be 6230 RPM and from the design point and Eqn. 14 the required power is 61.1 W. The flow torque required can therefore be found from $P = T_f \cdot \Omega$

$$T_f = 0.094 \text{ Nm} \quad (57)$$

This is the flow torque required for lossless flow assuming no windage and electrical losses from the motor, or other frictional losses. The delay between a vehicle disturbance and the motors responding to this disturbance, known as the control latency, must also be minimised to increase stability. Reducing the control latency will also reduce data noise when conducting hover tests as the power requirement from the motors will be more stable. Therefore the motors must possess sufficient torque to be able to rapidly respond to the control system. The moment of inertia of the rotor about it's rotation axis is found to be $I_{ZZ} = 51.01 \text{ kg} \cdot \text{mm}^2$ from a mass analysis of a CAD model of the rotor described above. The angular acceleration of the rotor can be described by

$$I_{ZZ}\dot{\Omega} + \frac{T_f(\Omega)}{\eta_r} = T_m(I) \quad (58)$$

Where η_r is a rotor efficiency. Taking the flow torque as constant and equal to the value obtained in Eqn. 57, the required motor torque, T_m is equal to

$$T_m = 51.1 \times 10^{-6} \cdot \dot{\Omega} + \frac{0.094}{\eta_r} \quad (59)$$

4.2.2 Power Supply

A 12V/84A (1kW) DC power supply is used to power the stationary propulsor tests and can be used in conjunction with a tether to provide flight power for hover tests. The flying test bed is also equipped to hold a 4-cell Li-Po with a nominal voltage of 14.8V to enable future dynamic testing. The 12V power supply is used to determine the motor requirements as it is the limiting factor.

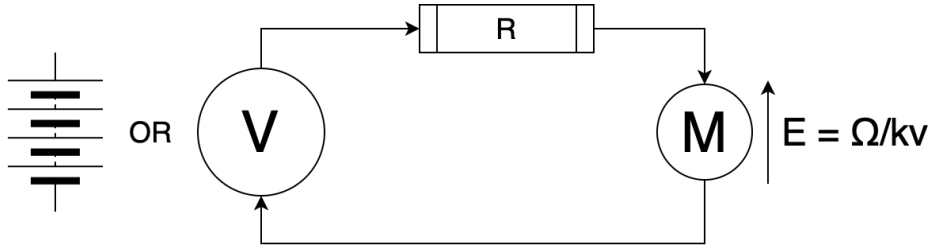


Figure 16: Electric motor model for DC/BLDC motors

4.2.3 Choice of Electric Motor

A brushless DC motor (BLDCM) can be modelled by the circuit in Fig. 16. The back-emf generated by the motor is proportional to the motor speed (as in Fig. 16) and the torque produced is proportional to the current, $T = 3k_t I_{phase} = \frac{\sqrt{3}I_{supply}}{k_v}$. The motor speed can be related to the electrical input quantities by

$$\Omega = (V - \frac{T_m k_v}{\sqrt{3}} R) \cdot k_v \quad (60)$$

Assuming linear acceleration from rest to demand speed and a maximum acceleration time of $75ms$, Eqn. 59 gives a maximum motor torque requirement of $T_m = 0.54 \text{ Nm}$. The motor is required to have an outer diameter no greater than $30mm$ to fit inside the hub with hub wall thickness of $5mm$. These requirements, are met by a Multistar Elite 2810-750kv BLDCM with internal resistance of 0.108 ohms . Rearranging Eqn. 60 gives an output torque at operating speed of

$$T_m = 0.76 \text{ Nm} \quad (61)$$

Allowing for a rotor efficiency of $\eta_r = 30\%$.

4.3 Mechanical Design

In this section the propulsor design is embodied and the mechanical aspects of the design considered.

4.3.1 Propulsor Dimensions

The rotor and stator profiles determined in Section 3.3 have a total axial chord of $52.5mm$ including a $12mm$ blade row gap. A blade duct length of $L = 60mm$ is chosen. Equation 21 and Eqn. 22 give values of $(r_c)_{EXIT} = 62.6mm$ and $(r_h)_{EXIT} = 17.4mm$. Table 3 shows the values of the remaining geometric variables. Figure 17 shows the embodiment of this design point. The propulsor design is modular allowing for part replacement and is comprised of 5 aerodynamic components and 1 electric motor (including rotor mount and spinner). The assembled propulsor has a length of $167mm$ and a maximum diameter (at the intake) of $180mm$. Design considerations for each component are discussed below.

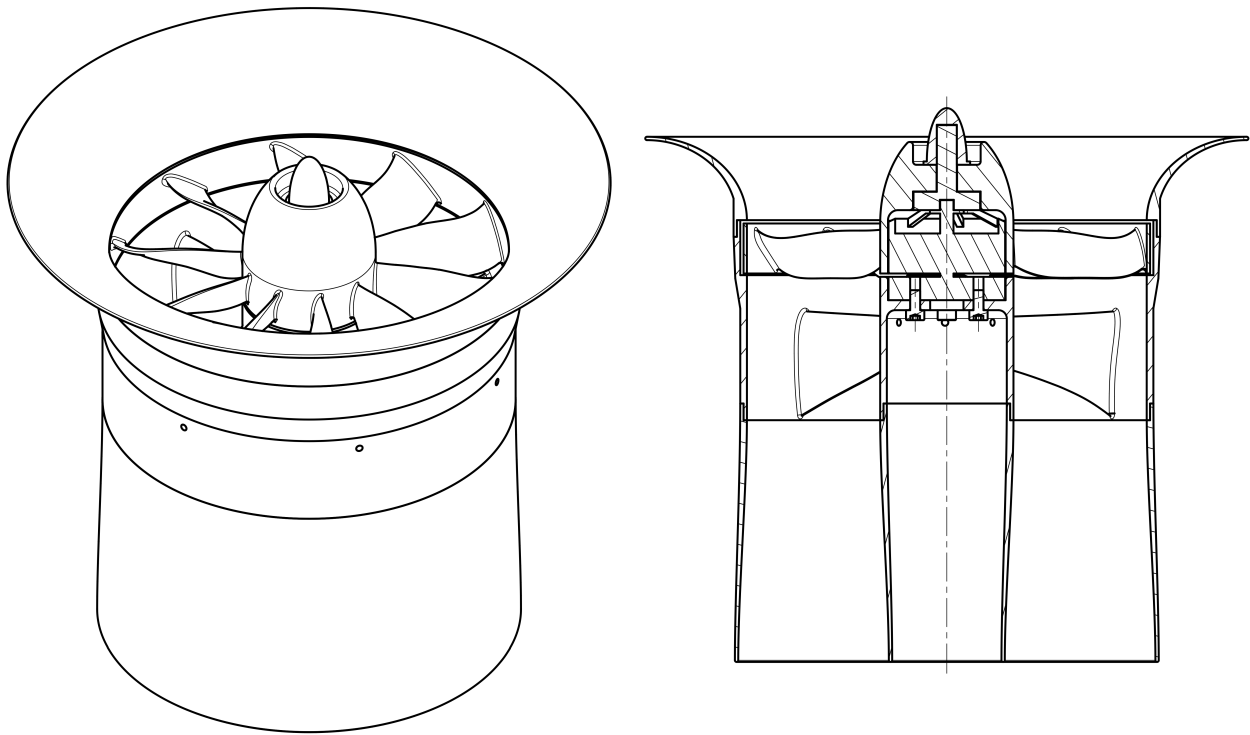


Figure 17: Isometric and section view of ducted fan design

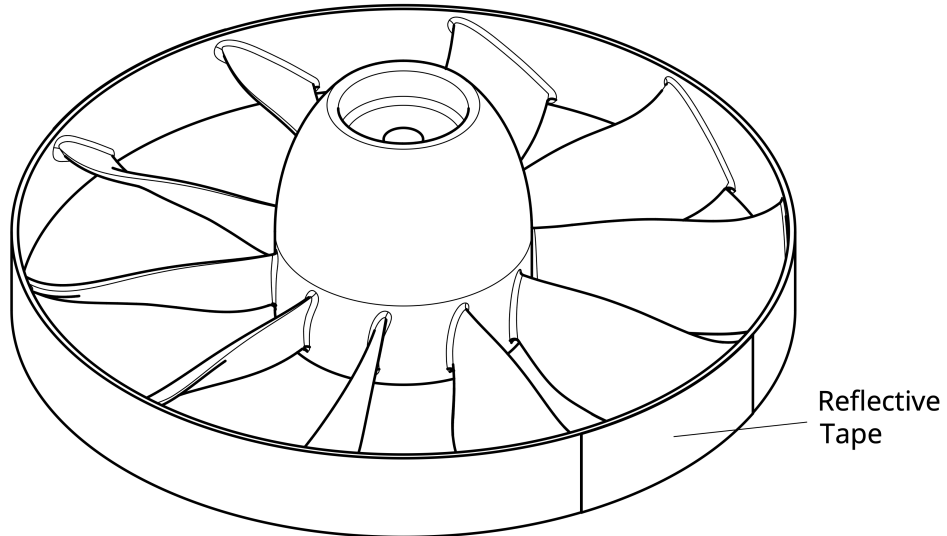


Figure 18: Isometric view of shrouded rotor

4.3.2 Shrouded Rotor

The rotor has 10 blades and is shrouded as in Fig. 18. The shrouding provides support for 3D printing to enable large overhangs without the blades deforming. The amount of

support material required is minimised as it can adversely affect surface finish of the blades. Reflective aluminium tape is mounted to the outside of the shroud and coupled with an IR photo-transistor mounted to the casing to enable measurement of the rotor speed. The clearances required to ensure an unshrouded rotor does not rub against the casing means the tip-gap required is large which introduces large losses due to tip-flows. Corner separations at the blade-shroud interface are minimised by adding lean to the blade as described in Section 3.3.6. To maintain a high quality printing finish on the trailing edge of the blade, print support must be avoided and so the blade is shifted in the axial direction to minimise the distance between the trailing edge and the build plate, located on a $r\text{-}\theta$ plane on the downstream side of the rotor. Maximum stress is expected at the blade-hub interface and so a fillet of 0.75mm is added to limit stress concentrations.

A finite element analysis (FEA) of the rotor at operating speed is undertaken. The rotor is fixed at the motor shaft and a centrifugal force is applied with equivalent rotor speed of $652\text{rad}\cdot\text{s}^{-1}$. A force of 5.5N is applied to the pressure side of the blades. 1st Order elements are used and the local mesh size at the blade hub is set to $\approx 0.1\text{mm}$. The von Mises yield criteria can be expressed as

$$\sigma_{yld} = \sqrt{3}k_{PLA} \quad (62)$$

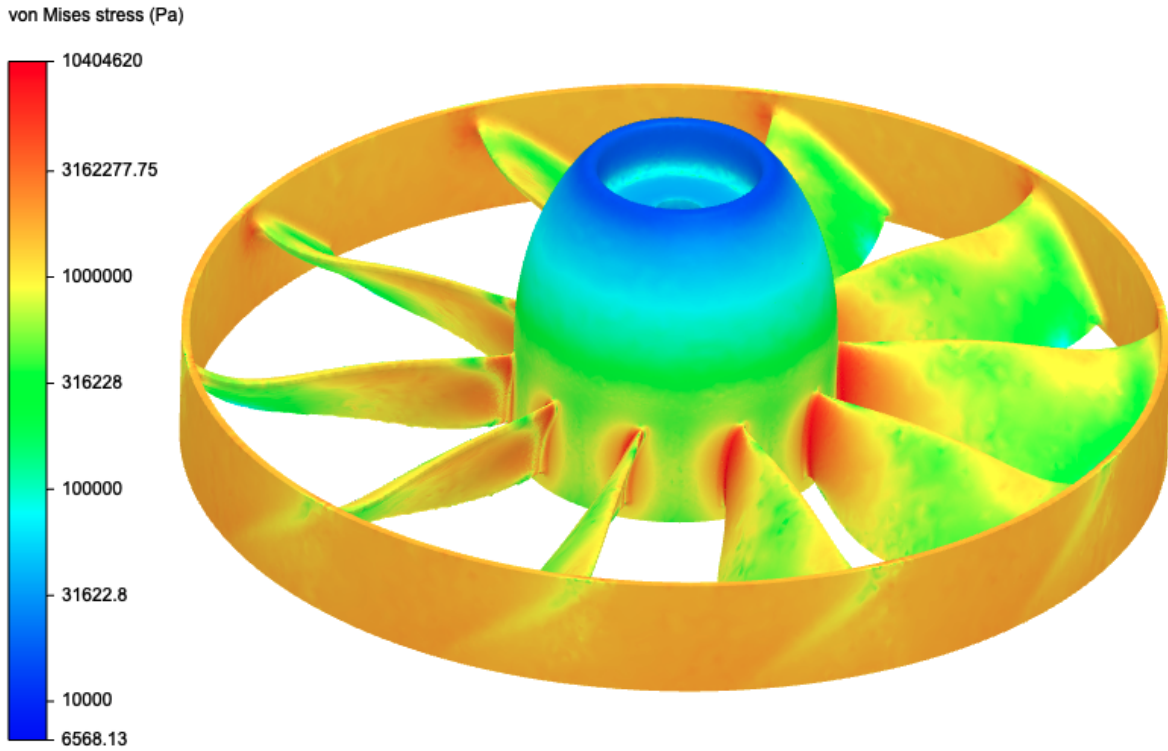


Figure 19: Finite element analysis of the rotor at operating speed with color bar showing von Mises stress with a logarithmic scale

Where $k_{PLA} = 33\text{ MPa}$ is the shear yield strength of 3D printed PLA as found by

Anderson (2017)[11]. This gives a maximum von Mises stress of $\sigma_{yld} = 57.2$ MPa. The FEA results in Fig. 19 show the maximum von Mises stress to be $\sigma_{vm} = 10.4$ MPa giving a yield margin of safety of

$$MS_{yld} = \frac{\sigma_{yld}}{\sigma_{vm}} - 1 = 4.5 \quad (63)$$

Radial displacement is negligible and so shroud clearance to casing is governed by 3D printing clearance values and shroud eccentricity as a result of 3D printing. The shroud has a thickness of 1mm and a shroud tip-gap of 1mm.

4.3.3 Stator Block: Stator and Blade Duct Hub & Casing

The stator blades are fixed to the blade duct hub and casing and are aerodynamic and structural components. The stators transfer the force of the fan to the drone chassis via the casing and arm. The stator, hub, and casing are 3D printed as one unit called the stator block as shown in Fig. 20. The electric motor mounts to part of the hub known as the mounting plate with 3x M3x6 cap-head bolts. The plate has ventilation holes that match the underside of the motor to allow airflow to cool the motor and prevent overheating. Though the motor is operating well below its rated power, maintaining airflow prevents the PLA expanding during operation which can cause warping and rubbing. The ventilation holes also allow the 3 power supply wires into the hub cavity below the mounting plate where they are connected to the three power supply cables. These power cables feed through from the flying test bed through passages in the stator blades that can be seen as holes on the casing in Fig. 20. These passages are generated by outputting the line of maximum blade thickness and lofting a circular section along it. The 3D printer generates minimum wall thicknesses of approximately 0.3mm so to avoid the passage breaking through the stator wall the loft diameter must be less than the maximum stator thickness minus $2 \times 0.3\text{mm}$. At the hub the maximum thickness is 2.15mm therefore the maximum passage width is $2.15 - 2(0.3) = 1.55\text{mm}$. This sets the limit for power supply wire thickness.

The hub provides an interference fit to the motor to reduce rotor eccentricity with respect to the casing. The intake and diffuser sections mount to the stator block with an interference fit. Both intake and diffuser casing are fixed in place with adhesive tape. The mounting point for the propulsor to be mounted to the flying test bed or the stationary test rig is sized to the outer dimensions of the load-cell. The arm attachment is shaped like the load-cell so the same pointing point can be used.

4.3.4 Diffuser

The diffuser is mounted to the stator block via an interference fit. The casing is also held in place with adhesive tape as it is more prone to detaching under vibration than the hub. Both diffuser hub and casing are designed to be as thin as possible while remaining rigid. At exit the diffuser has a thickness of 1mm and at entry it has a thickness of 2mm. Casing and hub sections can be printed simultaneously though this takes longer than printing one after the other and can reduce the flow-side surface quality.

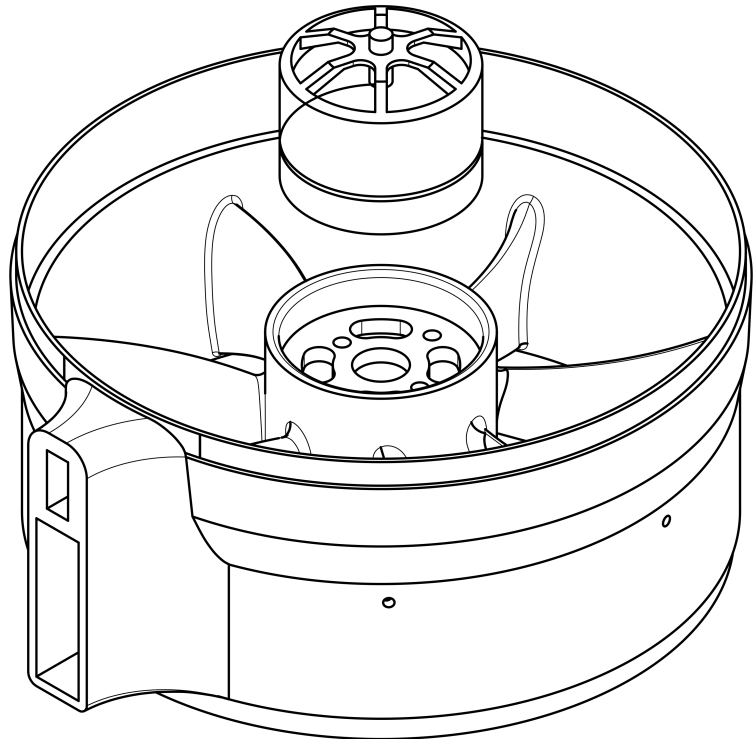


Figure 20: Exploded view of stator block and electric motor showing mounting plate with ventilation and mounting holes. Propulsor mounting point for mounting to flying test bed or stationary test rig is shown with mounting hole for IR photo-transistor

4.3.5 Intake

The intake is mounted to the stator block via an interference fit. As it generates thrust it must be securely attached to the stator block and so adhesive tape is also used. The intake is less prone to eccentricity as it is not straight or approximately straight. It can be printed with a constant thickness of 1mm. Print times for the intake can be large as significant support material is required due to the overhang of the lip.

4.3.6 3D Printing

All structural and aerodynamic parts are rapidly prototyped using an Ultimaker 3 3D printer and 2mm diameter RS Pro PLA filament. CAD models of parts are exported as `*.stl` files and sliced using Ultimaker CURA, outputting `*.gcode` files to be read by the printer. All parts are 3D printed in the Whittle Laboratory 3D printer room.

Tolerance: Prototyping test articles showed the printer to have the following approximate tolerances for various fit types when printing with 75% infill and cubic subdivision infill pattern.

Fit type	Approximate tolerance
Interference	$0.15mm$
Clearance (allowing for eccentricity)	$1mm$

Table 7: Tolerances for various fit types with 75% infill and cubic subdivision infill pattern on an Ultimaker 3

Component	Approximate build time
Rotor	13 hours
Stator block	1 day, 6 hours
Intake	1 day
Diffuser hub	3 hours
Diffuser casing	6 hours

Table 8: Approximate build times for propulsor components with 75% infill and cubic subdivision infill pattern on an Ultimaker 3

Build-plate Adhesion: The build-plate adhesion type ‘raft’ provided suitable adhesion for printing annular bladed structures. As the trailing edges of the blades are thin (≈ 1 line width) adhesion is poor. This can be solved by using a raft and reducing the parameter ‘Raft Air Gap’ to ensure good adhesion between the raft and the first layer of the model.

Build Times: Table 8 outlines the approximate build time for each of the components described allowing an approximate estimate to be made for total build time.

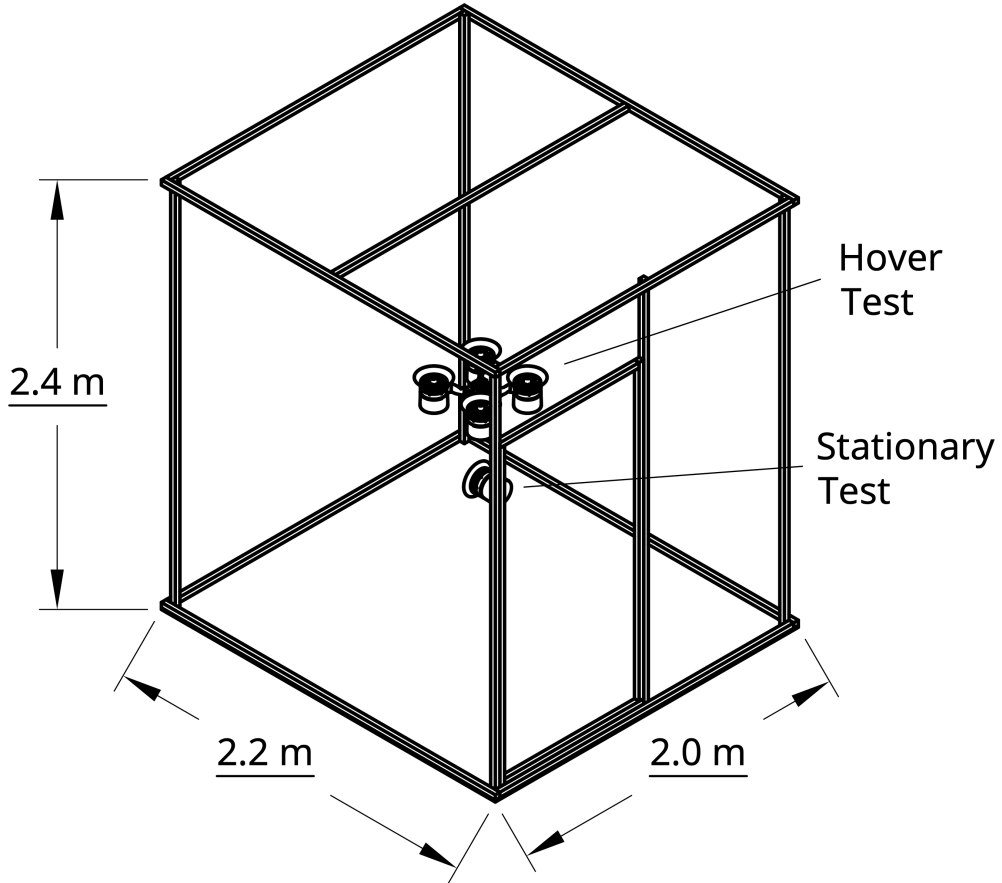


Figure 21: Test cage shown in isometric view with flying test bed in hover test configuration and an individual propulsor in the stationary test position (stationary test mount not shown)

Experimental Methods

Two types of experiment are undertaken: stationary propulsor tests; hover tests to determine system performance. All testing is done in a purpose built indoor test environment at the Whittle Laboratory. Figure 21 shows the $2.0m \times 2.2m \times 2.5m$ cage constructed with $3cm \times 3cm$ timber beam and $1cm$ grid chicken wire covering the sides to provide protection from the propulsor and flying test bed.

5.1 Stationary Propulsor Test

Propulsor performance is tested on the stationary test rig, shown in Fig. 22, to determine thrust, power, RPM, and motor temperature as well as characterise the aerodynamic performance with static pressure measurements. Thrust is measured by a single ended shear beam load-cell mounted on the casing perpendicular to the axis of the fan. RPM can be determined using the IR photo-transistor mounted on the casing, and the reflective tape on

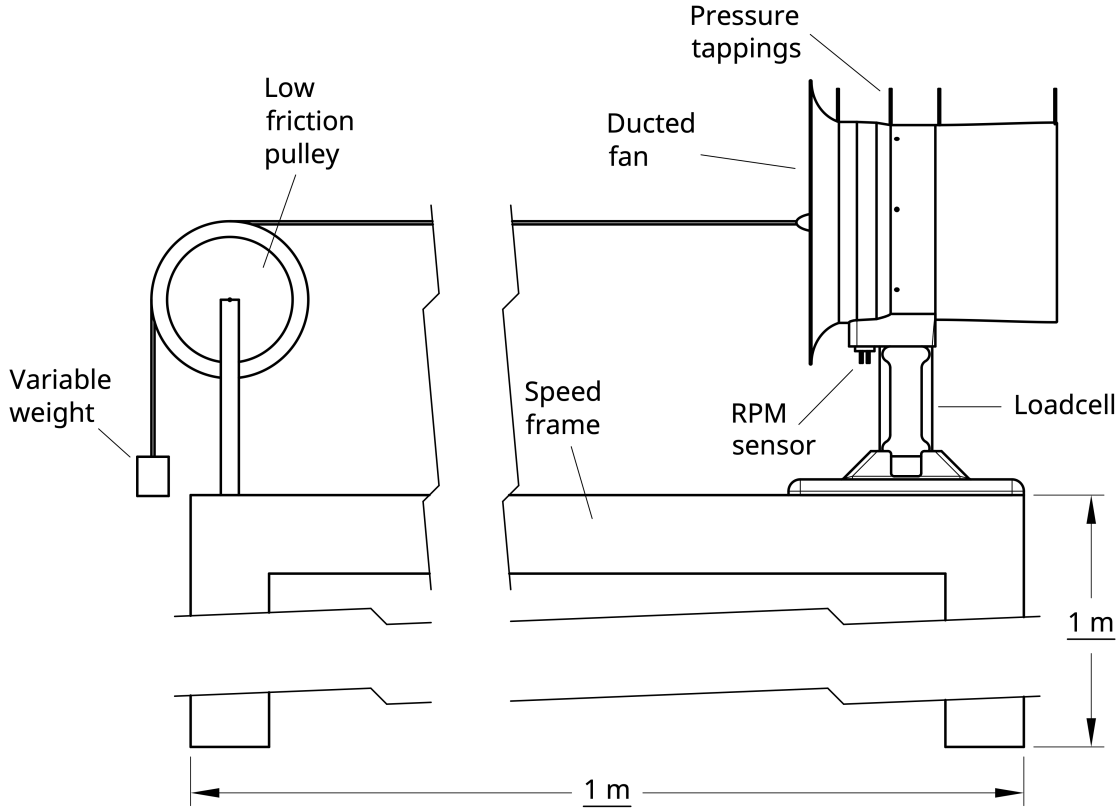


Figure 22: Experimental setup of stationary tests in calibration configuration

the outside of the rotor shroud. Power is determined from DC voltage and current output readings from the flight controller. K-type thermocouple measures the temperature at the base of the motor. Pressure tappings on the casing of the fan allow the static pressure to be determined at various axial positions along the propulsor. All electronic connections are made using metallic braid shielded cable. Thrust, power, and RPM data is collected by the flying test bed chassis and the main motor outputs are used to power and control the propulsor. Temperature readings are made using an external thermometer.

5.1.1 Setup

Figure 22 shows the experimental setup for stationary tests in the calibration configuration. An aluminium speed-frame structure is fixed to the ground and has a horizontal mounting position 1m in height and 1m in length. Thrust, RPM, temperature and pressure measurements require external sensors; their setup is described below. The flying test bed requirements for stationary testing is also described.

Load-cell: The propulsor is mounted at one end of the frame via a 0.6kg rated single ended shear beam load-cell. A low friction pulley is mounted to the other end of the frame with the top of the pulley in line with the axis of the fan. Light-weight high tensile fishing wire is at-

tached to the rotor spinner and is fed over the pulley, attaching to a vertically hanging weight that is used to calibrate the load-cell. This weight can be varied in multiples of $50g$ up to $500g$. When testing, the wire is detached from the spinner and secured so as not to interfere with the fan. The load-cell connects through an HX711 ADC/amplifier breakout board that is mounted to the frame. Data is transmitted from the HX711 to the GPIO pins of the RPi3.

IR Photo-transistor: The IR photo-transistor inserts into an interference fitted slot above the mounting point, as in Fig. 22. A small potential divider circuit is connected to the output of the photo-transistor and is connected to the 5V DC/Ground and GPIO pins of the RPi3 via the shielded cable.

Thermocouple: The K-type thermocouple is fixed with super glue to the motor mounting plate in the propulsor hub with the sensing junction resting against the base of the motor. The other end is fed through a hollow stator and is plugged into a K-type thermocouple external thermometer from which temperature readings are taken.

Pressure Transducers: $1.1mm$ holes are drilled radially into the casing at 4 axial locations as in Fig. 22: upstream of the rotor; upstream of the stator, mid blade passage; downstream of the stator, mid blade passage; exit from exit duct. $1.1mm$ outer diameter hypodermic tube tappings are inserted into the holes and secured with super glue on the outside of the casing, ensuring the tapping does not protrude out into the flow on the duct side of the casing. Plastic tubing with $1mm$ inner diameter is fixed to the end of the tappings and connected to input ports of a 16-channel DSA. The DSA is connected via an Ethernet switch to the control computer from which gauge pressures (relative to ambient) can be read.

5.1.2 Load-cell Calibration

The load cell must first be calibrated in order to determine the thrust developed by the propulsor. The setup described above allows multiple readings to be made within the load-cell's operating range. 10 different forces are applied to the propulsor using the $50g$ weights and the mean of 100 readings taken at each force. The resulting data points are plotted in MATLAB and a curve is fit to the result. The data is linear in the full range of operation of the load-cell.

5.2 Hover Test

Hover tests are undertaken in the test environment by mounting propulsors to the flying test bed and conducting a static hover from a top-down tether. The hover test determines the figure of merit in flight, the noise levels produced, and the vehicle stability in hover and compares the values for the ducted fan with a hover optimised propeller.

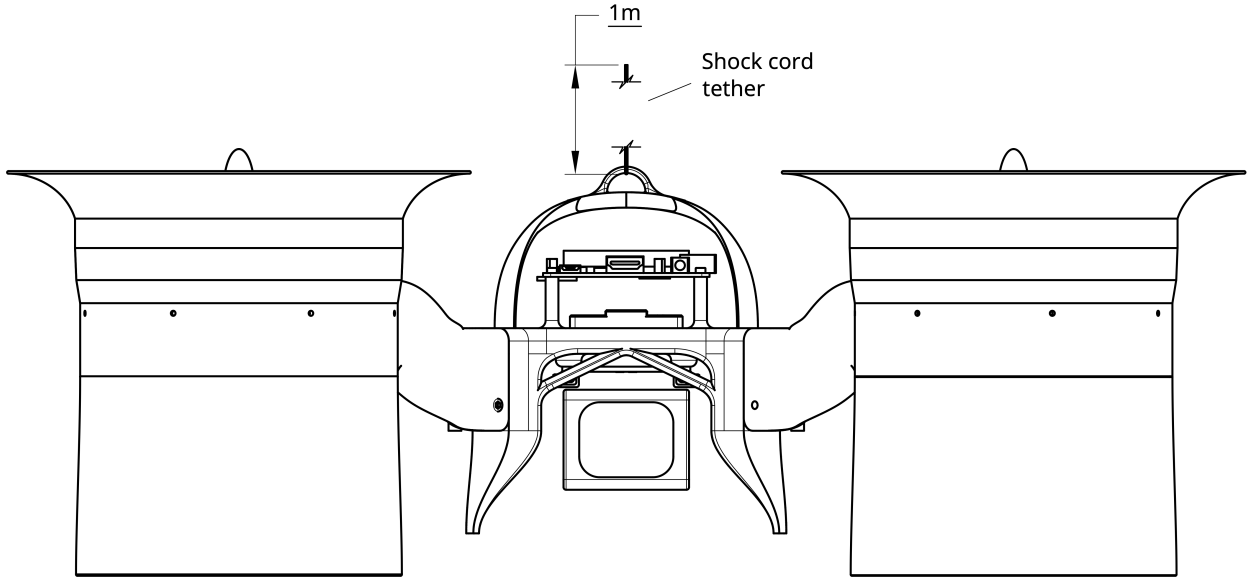


Figure 23: Front view of flying test bed in hover configuration

5.2.1 Setup

The tether ensures the flying test bed is clear of the ground to reduce any ground effect. The tether is made of 1m of shock cord (slack) to ensure reduce stress on the structure in the event of a sudden loss in power or emergency situation in which the propulsors must be shutdown. To attach the tether to the flying test bed and act as a roll cage in the event of a collision with the topside of the chassis, an arched frame can be mounted to the chassis as in Fig. 23. A single RPM sensor is used during hover tests to ensure the RPi3 sample rate on the IR photo-transistor output is high enough to register the two reflective strips on the rotor shroud each revolution.

RPM: At operating speeds, one revolution of the rotor takes $9.63ms$. Each reflective strip is $50mm$ in length (with negligible thickness) and is attached to the outside face of the shroud at a radius of $r_c + 1mm$ and so takes $[50/(2\pi(r_c+1))] \times 9.63ms = 1.26ms$ for the tape to pass the IR photo-transistor. Therefore the minimum sample rate for the IR photo-transistor to register the tape is $1/1.26ms \approx 800Hz$. In order to make the reading more reliable and ignore spurious reflections it is determined that 10 consecutive readings are required to register the tape and ignore errors. This increases the minimum sample rate to $8000Hz$. Allowing for 200% operating motor speed during stationary propulsor tests increases this requirement to $16kHz$. The RPi3 was found to have a GPIO sample rate of $30kHz$ therefore recording RPM from 2 propulsors would require a sample rate above this. Assuming negligible variation in electric motor and propulsor performance, all 4 propulsors should operate at a similar RPM during static hover.

Noise: Acoustic noise generated by the flying test bed are measured by the internal micro-

phone on a mobile device kept at a horizontal distance of approximately 1m. This allows the noise output by the ducted fan and the propellers to be compared.

5.2.2 Control

The Pixhawk 4 flight controller altitude hold mode attempts to maintain the current altitude and position using its onboard GPS, accelerometers, and gyros. The indoor test environment reduces the GPS accuracy and so manual corrections are made using a handheld radio transmitter. Automatic position holding is possible using the forward-right-down ultrasound sensor array.

5.3 Measurement Techniques

Numerous measurements are made to quantify the performance of the propulsor. These measure: the overall performance in terms of the figure of merit, power required and thrust; aerodynamic performance in terms of pressure coefficients, flow coefficient and stage loading; noise levels produced by various propulsors.

5.3.1 Non-dimensional Quantities

Figure of Merit: Figure of merit is found using measured or equivalent thrust and electrical power requirement. Thrust is measured directly using the load-cell in the stationary tests but in the hover tests the thrust is taken as being equal to the flying test bed mass, which is measured prior to flight using a high precision scale. Both load-cell and scales have a accuracy of $\pm 0.1g \approx \pm 0.1mN$. A Python script on the RPi3 manages simultaneous recording of thrust (from load-cell) and RPM (from IR photo-transistor data) and produces a *.txt log file that is wirelessly imported to MATLAB via the SCP protocol. Power is measured using the Pixhawk 4 measured current and voltage output. Maximum sample rate is $\approx 1Hz$ and so 30 readings are made. An instantaneous power is calculated at each data point and a mean power is calculated. Readings are accurate but due to noise, particularly during hover tests, they can be imprecise. Taking a mean value over a large window reduces the effect of noise. Voltage and current data is obtained through the logging feature on QGroundControl: MavLink Inspector. The recorded log can be imported into MATLAB for processing. The flow area is assumed as designed ($A_x = \pi(r_c^2 - r_h^2)$) and air density is taken as $\rho = 1.225kgm^{-3}$.

Flow Coefficient:

Stage Loading: Total-static pressure rise...?

Diffuser Static Pressure Recovery:

5.3.2 Data Acquisition

Acquisition and integration of systems and software.

5.3.3 Cage Design & Tether

Results

6.1 Stationary Propulsor Test

6.1.1 Comparison of Vortex Distributions

6.1.2 Version 1.0 EDF

Heavy Blue: 3 exits and 3 rotor vortex designs. Comparison of intake performance (long and short).

- Power (Current and Voltage)
- Thrust
- FOM
- RPM

6.1.3 Version 2.0 EDF

1 exit and 2 rotor vortex designs. Long intake only.

- Power (Current and Voltage)
- Thrust
- FOM
- RPM
- Pressures

6.1.4 Version 3.0 EDF

1 exit and 1 rotor vortex designs. Long intake only.

- Power (Current and Voltage)
- Thrust
- FOM
- RPM
- P1 Only

6.1.5 Propeller

6.2 Hover Tests

6.2.1 Propeller Performance

6.2.2 Hover Test Limitations

Future Work

Future work can be a proper section

Do the hover tests

Manoeuvre tests

- Look at what the Mf vs manoeuvre metric would look like

- What could the manoeuvre metric look like?

Actual theory on contra-rotating

7.1 Propulsor Design

7.1.1 Stationary Propulsor Tests

What else would I have done to finish these off?

7.1.2 Contra-rotating Ducted Fan

Motivation for CR design More smaller motors better? CAD of what it might look like.
Velocity triangles ie Do the design and see how it would work theoretically.

7.1.3 Computational Fluid Dynamics

- Discuss limitations of design method (with respect to previous sections on deviation etc.)
- Reference Megs work? Show that CFD can get close to experimental results ie prove the method.

7.2 Flying Test Bed Experiments

How to quantify manoeuvre stability? The ‘Eriksen’ manoeuvre?

Conclusions

References

- [1] A. Maffioli, C. Hall, and S. Melvin, “Aerodynamics of low reynolds number axial compressor sections”, in *53rd AIAA Aerospace Sciences Meeting*, 2015, p. 1934.
- [2] R. Corralejo and P. Harley, “Smith diagram for low reynolds number axial fan rotors”, in *12 th European Conference on Turbomachinery Fluid dynamics & Thermodynamics*, EUROPEAN TURBOMACHINERY SOCIETY, 2017.
- [3] E. S. D. Unit, “Performance of circular annular diffusers in incompressible flow”, Engineering Sciences Data Unit, Tech. Rep., 1975.
- [4] J. Barry, “4th year project report: Propulsion systems for vtol electric vehicles”, Cambridge University Engineering Department, Tech. Rep., Jun. 2019.
- [5] S. L. Dixon and C. Hall, *Fluid mechanics and thermodynamics of turbomachinery*. Butterworth-Heinemann, 2013.
- [6] S. Lieblein, F. C. Schwenk, and R. L. Broderick, “Diffusion factor for estimating losses and limiting blade loadings in axial-flow-compressor blade elements”, NATIONAL ADVISORY COMMITTEE FOR AERONAUTICS CLEVELAND OH LEWIS FLIGHT . . . , Tech. Rep., 1953.
- [7] A. R. Howell, “Fluid dynamics of axial compressors”, *Proceedings of the Institution of Mechanical Engineers*, vol. 153, no. 1, pp. 441–452, 1945.
- [8] A. Howell, “Design of axial compressors”, *Proceedings of the Institution of Mechanical Engineers*, vol. 153, no. 1, pp. 452–462, 1945.
- [9] A. D. Carter, *The low speed performance of related aerofoils in cascades*. HM Stationery Office, 1950, vol. 29.
- [10] J. V. Taylor and R. J. Miller, “Competing Three-Dimensional Mechanisms in Compressor Flows”, *Journal of Turbomachinery*, vol. 139, no. 2, Oct. 2016, 021009, ISSN: 0889-504X. DOI: 10.1115/1.4034685. eprint: https://asmedigitalcollection.asme.org/turbomachinery/article-pdf/139/2/021009/6305774/turbo_139_02_021009.pdf. [Online]. Available: <https://doi.org/10.1115/1.4034685>.
- [11] I. Anderson, “Mechanical properties of specimens 3d printed with virgin and recycled polylactic acid”, *3D Printing and Additive Manufacturing*, vol. 4, no. 2, pp. 110–115, 2017.

Appendix A: COVID-19

Appendix B: Derivations

Velocity triangles?

Temporary Appendix Figures

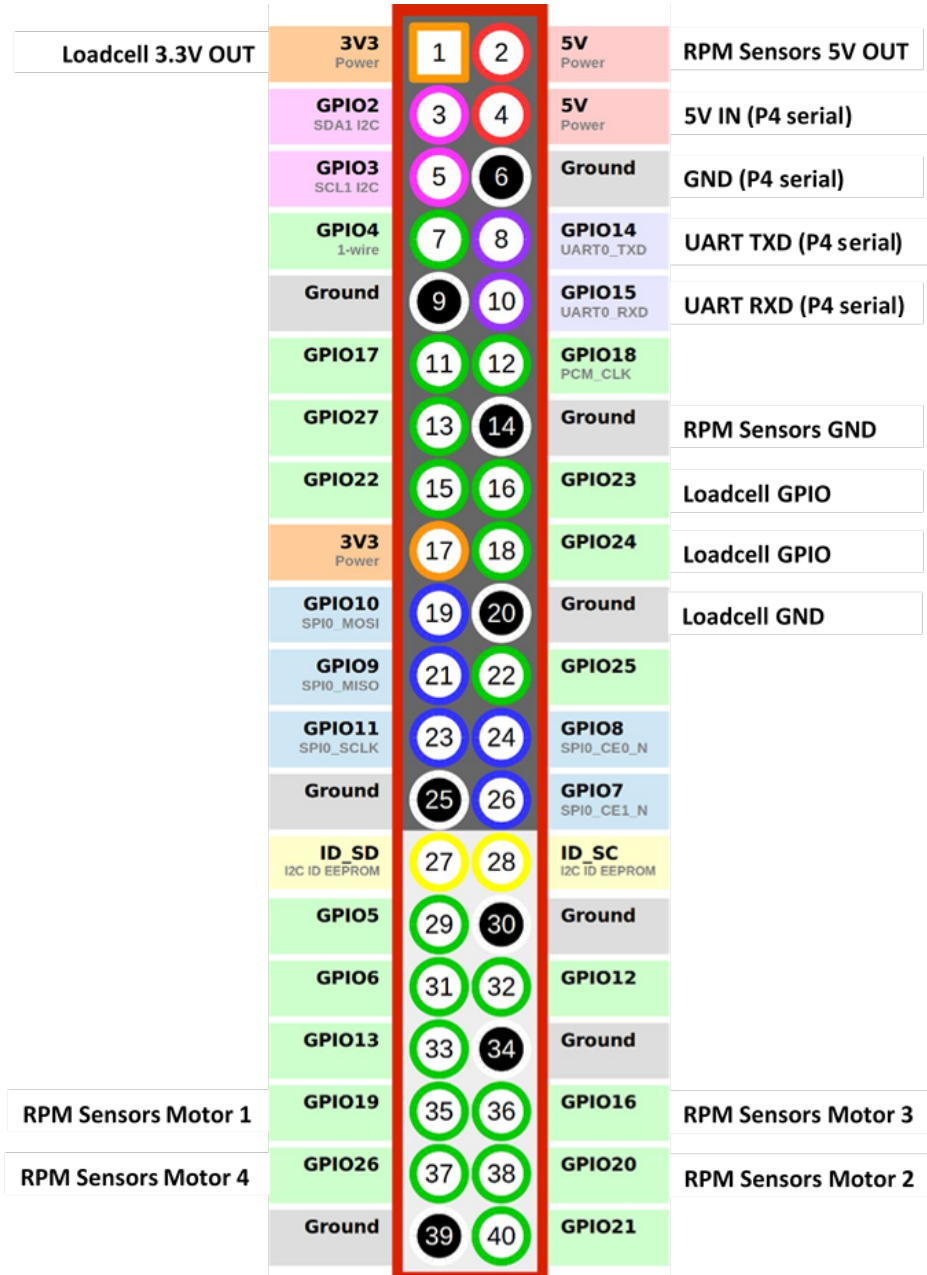


Figure 24: RPi3 header board with labelled used pins

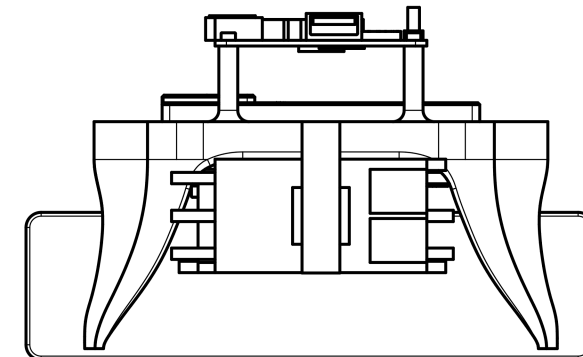
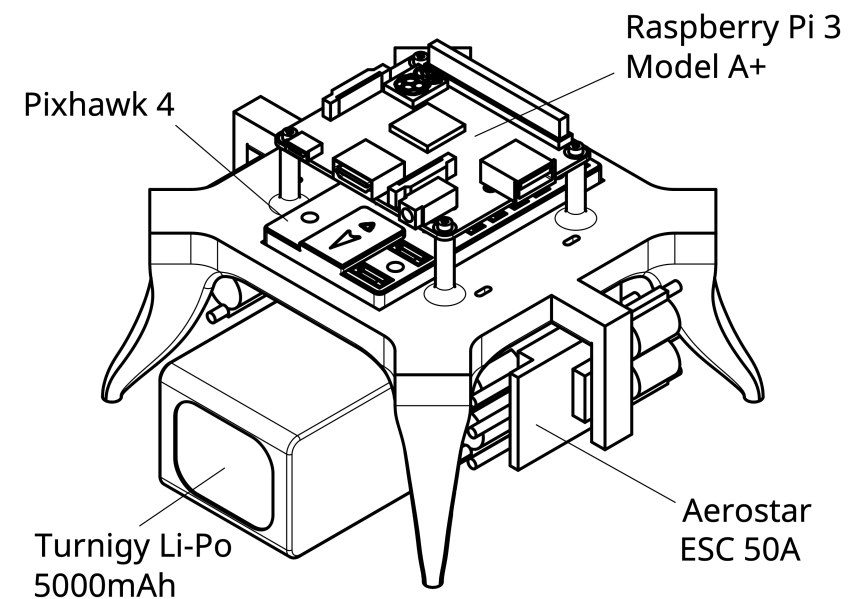
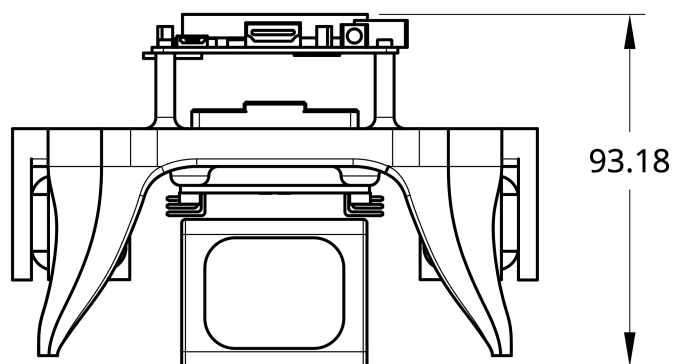
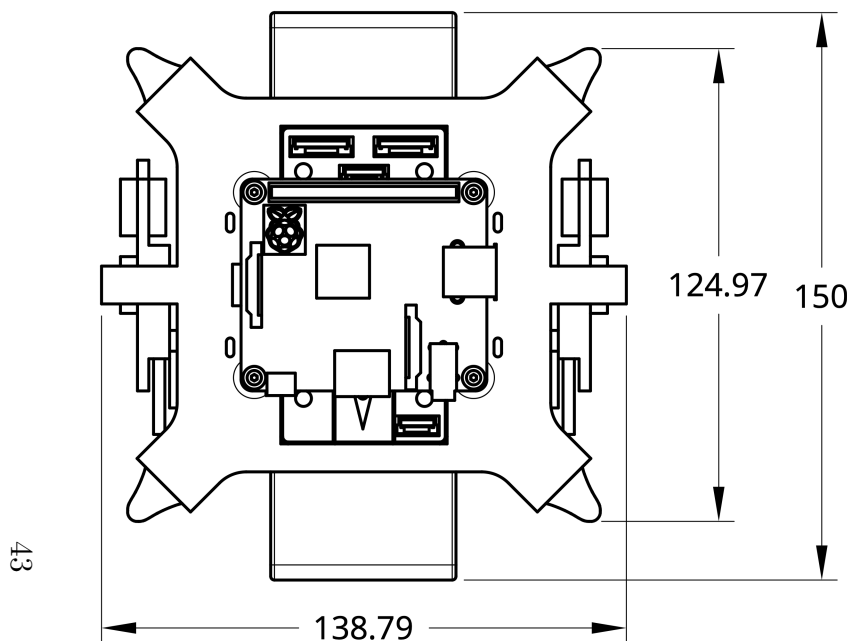


Figure 25: 3rd Angle projection of flying test bed chassis with principal dimensions and an isometric view